

ADVANCED FUNCTIONAL MATERIALS

Supporting Information

for *Adv. Funct. Mater.*, DOI: 10.1002/adfm.202108392

Interplay of Structure, Charge-Carrier Localization
and Dynamics in Copper-Silver-Bismuth-Halide
Semiconductors

*Leonardo R. V. Buizza, Harry C. Sansom, Adam D.
Wright, Aleksander M. Ulatowski, Michael B. Johnston,
Henry J. Snaith,* and Laura M. Herz**

Supporting Information:
Interplay of structure, localisation and
charge-carrier dynamics in
copper-silver-bismuth-halide semiconductors

Leonardo R. V. Buizza,[†] Harry C. Sansom,[†] Adam D. Wright,[†] Aleksander M.
Ulatowski,[†] Michael B. Johnston,[†] Henry J. Snaith,^{*,†} and Laura M. Herz^{*,†,‡}

[†]*Department of Physics, University of Oxford, Clarendon Laboratory, Parks Road, Oxford,
OX1 3PU, United Kingdom*

[‡]*TUM Institute for Advanced Study, Lichtenbergstraße 2 a, 85748 Garching bei München,
Germany*

E-mail: henry.snaith@physics.ox.ac.uk; laura.herz@physics.ox.ac.uk

Contents

1	Sample Fabrication	S-3
2	Experimental Methods	S-5
3	Compositional Analysis and X-Ray Diffraction	S-7
4	Fitting of Optical Absorption Spectra Using Elliott's Theory	S-14
5	THz and Infra-Red Dielectric Function	S-16
	Silver-bismuth-iodide lattice response is similar to that of MAPbI ₃	S-16
5.1	Calculation and modelling of dielectric function in the THz frequency range .	S-18
5.2	Calculation of the dielectric function in the infra-red	S-21
6	PL Stability Under Continuous Illumination	S-24
7	Photoluminescence and Time-Correlated Single-Photon Counting	S-24
8	THz Photoconductivity	S-27
	Drude Factor Calculation	S-27
9	Fitting of OPTP Decays	S-30
	Early-time OPTP fitting	S-30
	Long-time (nanosecond) OPTP fitting	S-32
10	Instrument Response of OPTP Spectroscopy	S-36
11	Fluences, Photon Fluxes and Photoexcited Charge-Carrier Densities for OPTP Measurements	S-37
	References	S-40

1 Sample Fabrication

AgI, Bi and I₂ powders (Table 1) were dissolved in 0.8 ml dimethyl sulfoxide (DMSO) by stirring at 140 °C for 15 minutes. In a separate vial CuI powders were dissolved in pyridine by stirring at 140 °C for 15 minutes. The CuI in pyridine solution was quickly filtered through a 0.22 µm pore-size, 13 mm diameter PTFE filter and added to the AgBiI in DMSO solution. The Cu-Ag-Bi-I in DMSO and pyridine solution was stirred for another 15 minutes at 140 °C. The solution was filtered through a 0.22 µm pore-size, 13 mm diameter PTFE filter and left to keep stirring at 100 °C during deposition.

Glass microscope slides cut to size (approx. 24 mm × 24 mm) and z-cut quartz substrates were sonicated in soap and de-ionised (DI) water for 15 minutes, rinsed with DI water, sonicated in acetone for 15 minutes, sonicated in IPA for 15 minutes, dried using an N₂ gun, and then further cleaned in a UV-Ozone generator for 10 minutes. Following this, the substrates were quickly transferred to a N₂-filled dry box and kept at 150 °C for deposition. 100 µl of the 100 °C Cu-Ag-Bi-I solution was deposited dynamically onto the 150 °C substrate and spun at 4000 rpm for 45 seconds on a spincoater. The films were then annealed at 50 °C for 30 minutes in air, during which the films turned from a clear orange film to a dark red-brown film. The film was then annealed at 150 °C for 5 minutes in air. Films were kept in a nitrogen-filled glovebox until needed for measurements. The films deposited on the z-cut quartz substrates were used for optoelectronic characterisation. The films deposited on microscope slides were used to take microscopy images and compositional measurements using scanning electron microscopy (SEM) energy-dispersive X-ray (SEM-EDX) analysis. XRD was used to identify the phases present in the films, and to compare between the films deposited on microscope slides and z-cut quartz. Z-cut quartz was chosen owing to its high transparency in the THz frequency range.^{S1}

Table S1: Summary of material and solvent amounts used to create solutions for each of the five $\text{Cu}_{4x}(\text{AgBi})_{1-x}\text{I}_4$ compositions investigated.

Nominal x and composition	Solution 1				Solution 2	
	AgI (mg)	Bi (mg)	I ₂ (mg)	DMSO (ml)	CuI (mg)	Pyridine (ml)
0, AgBiI ₄	157	139	254	0.8	0	0.22
0.09, Cu _{0.4} AgBiI _{4.4}	157	139	254	0.8	51	0.32
0.2, CuAgBiI ₅	157	139	254	0.8	127	0.48
0.33, Cu ₂ AgBiI ₆	157	139	254	0.8	254	0.74
0.6, Cu ₆ AgBiI ₁₀	157	139	254	0.8	762	1.77

2 Experimental Methods

UV-Visible Absorption: UV-Visible absorption spectra were taken using a Perkin Elmer Lambda 1050 spectrometer with an integrating sphere accessory. Deuterium and halogen lamps were used as light sources for the UV, and visible and near-infrared spectral ranges, respectively. A photomultiplier tube and lead sulfide detector were used for light detection for the UV and visible, and near-infrared ranges, respectively.

In order to calculate the absorption coefficient, the following formula was used:

$$\alpha = -\frac{1}{d_{\text{sam}}} \ln \left(\frac{T}{1 - R} \right). \quad (1)$$

Here $T = t_{\text{sam}}/t_{\text{reference}}$, $R = r_{\text{sam}}/r_{\text{reference}}$, and d_{sam} is the thickness of the thin film. Thicknesses were measured using a Veeco Dektak 150 profilometer.

X-Ray Diffraction: X-Ray Diffraction patterns were measured using a PANalytical X'Pert powder diffractometer, using radiation from a Cu-K $_{\alpha 1}$ source, across 2θ values ranging from 5 – 45°. TOPAS-Academic V6 was used to perform Pawley fitting. In order to correct against sample tilt, the z-cut quartz peak at $2\theta = 16.43^\circ$ was used as a reference to pin the spectra measured on quartz substrates.

Steady-State Photoluminescence Spectra: Samples were photoexcited by a 398 nm diode laser (Picoquant, LDH-D-C-405M) with an intensity of 265 Wcm $^{-2}$ on the sample. The resultant photoluminescence (PL) was collected and coupled into a grating spectrometer (Princeton Instruments, SP-2558), which directed the dispersed PL onto a silicon iCCD (Princeton Instruments, PI-MAX4). Measurements were carried out in a nitrogen atmosphere.

Time-Correlated Single-Photon Counting: Time-resolved PL decays were measured using Time-correlated single-phonon counting (TCSPC) following excitation by a 398-nm pulsed laser (Picoquant, LDH-D-C-405M). The emitted PL was collected and coupled into a grating spectrometer (Princeton Instruments SP-2558), after which light was detected by a photon-

counting detector (PDM series from MPD). The measurements were carried out with a repetition rate of 2.5 MHz at fluences of 1580 and 440 nJcm⁻², and timing was controlled electronically using a PicoHarp300 event timer. PL decays were measured in a nitrogen atmosphere at the peak wavelength of the measured PL spectra.

Time-resolved emission spectroscopy (TRES) measurements involve carrying out TCSPC measurements across a range of wavelengths (at a set interval). For the TRES measurements the same setup as above was used, but with a repetition rate of 10 MHz and an excitation fluence of 1610 nJcm⁻². These measurements were also carried out in a nitrogen environment.

Optical Pump Terahertz Probe Spectroscopy: An amplified laser system (Spectra Physics, MaiTai - Ascend - Spitfire) with a central wavelength 800 nm, 35-fs pulse duration and 5 kHz repetition rate was used to generate THz radiation via the inverse spin hall effect^{S2} and was detected using free-space electro-optic sampling with a 1 mm-thick ZnTe (110) crystal, a Wollaston prism and a pair of balanced photodiodes. The THz pulse was measured in transmission geometry, and measurements were carried out under vacuum ($< 10^{-2}$ mbar).

To obtain a pump wavelength of 400 nm, the pump beam was frequency-doubled to 400 nm by a β -barium-borate (BBO) crystal. To obtain pump wavelengths of 500 and 585 nm, output from an optical parametric amplifier (Light Conversion: TOPAS-C) was used, pumped with 800 nm-wavelength excitation from the amplified laser system described above.

For the THz dark conductivity measurements, the same setup was used, with only the THz probe beam being used (i.e. without photoexcitation).

3 Compositional Analysis and X-Ray Diffraction

As an initial characterisation, scanning electron microscopy (SEM) images were taken for the five $\text{Cu}_{4x}(\text{AgBi})_{1-x}\text{I}_4$ compositions investigated here, which had been deposited as thin films onto glass microscope slides (see Figure S2). The images show a clear trend in film morphology with composition, with film coverage decreasing monotonically as x increases. This increase in film roughness is likely to lead to stronger scattering of light in the optical range, potentially contributing to the stronger apparent sub-band gap absorption features measured by light transmission through the thin films (shown in Main Figure 1 (b) and Figure S6).

Along with the images, compositional analysis of the films was carried out *via* SEM-EDX measurements, using CuI, AgI and BiI_3 powders as reference standards. The results of the compositional analysis are plotted on a triangle plot in Main Figure 1 (a), and as a histogram of measured compositions along the $\text{AgBiI}_4 - \text{CuI}$ solid solution line in Figure S1. The measurements show that the compositions of the films deposited on microscope slides are in excellent agreement with the nominal, expected compositions, although, as seen on the triangle plot, all films have a slight iodine deficiency: we attribute this to the formation of a BiOI impurity phase, which is detected in the X-ray diffraction (XRD) measurements for the films deposited on glass microscopy slides (discussed below). However, the lack of such an impurity phase in the XRD measurements for the films deposited on quartz (which were used for all optoelectronic measurements) gives us some confidence that the iodine deficiency will not be significant in those films.

The X-ray diffraction (XRD) patterns of thin films deposited on quartz substrates are shown in Figure S3. We performed Pawley fits on the XRD data, using the beneficial reference peaks from the quartz substrates (marked with asterisks in Figure S3) as an internal standard to compare the relative lattice parameters and unit cell volumes of the series of investigated phases. The presence of the XRD peaks arising from the z-cut quartz at $\sim 16^\circ$ and $\sim 33^\circ$ are not expected from the reported structures of quartz in the Inorganic Crystal

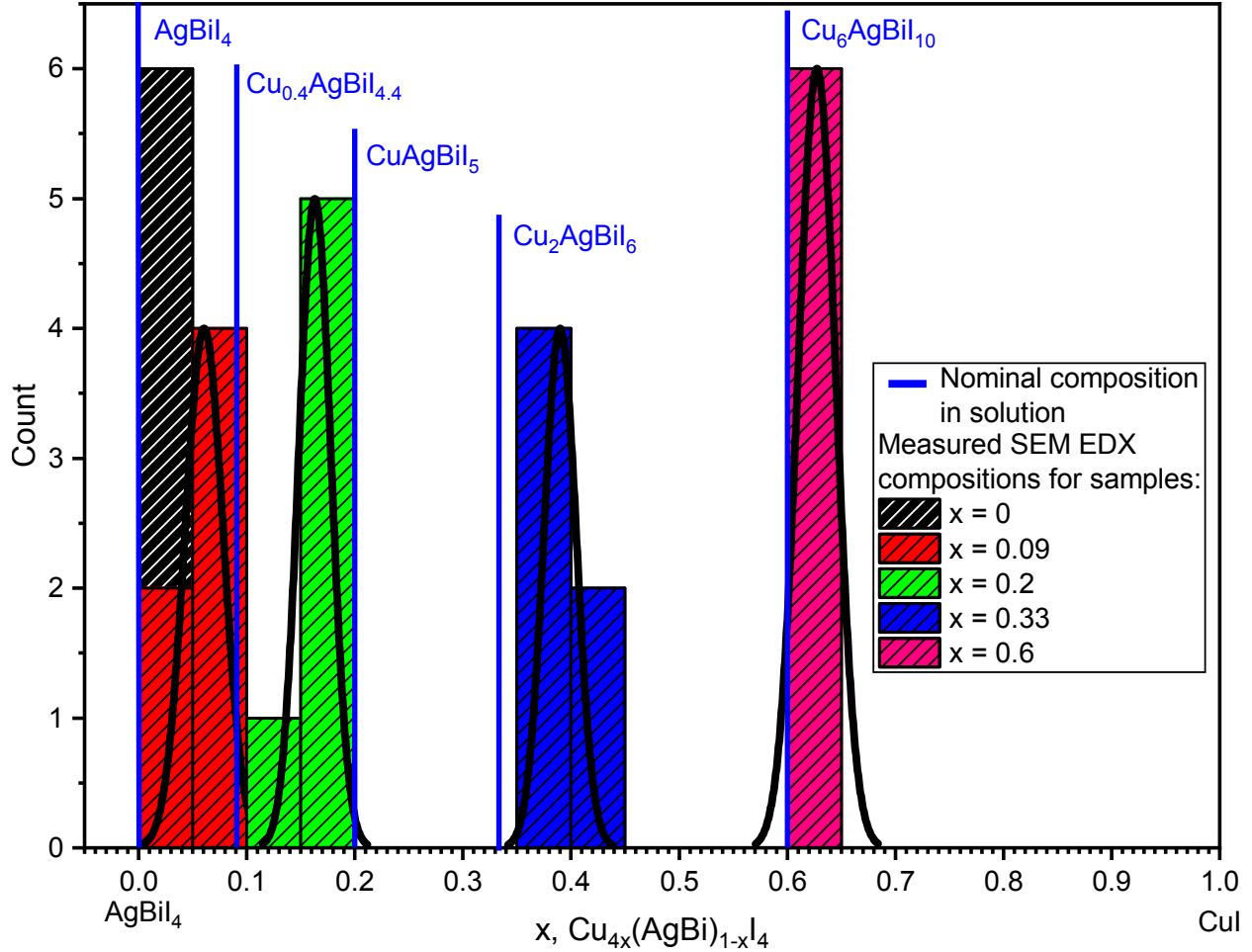


Figure S1: The distribution of x values measured for each film by SEM EDX, compared to the nominal composition in the solution. These values were measured for films deposited on microscope slides. (There is no Gaussian distribution for $x = 0$ as there was no copper included in this material, giving no variation along the $\text{AgBi}_4 - \text{CuI}$ solid solution line. Variations in silver and bismuth content for this composition are shown in Figure 1 in the main text.)

Structure Database (ICSD). However, the d-spacings of these peaks do correspond to the c-lattice parameter of the low temperature alpha SiO_2 phase.^{S3} Therefore, the substrate peaks were fitted by the $h00$ reflections of a phase in an arbitrary cubic space group $Pm\bar{3}m$. The refined lattice parameter of $5.408(2) \text{ \AA}$ was then fixed for the fitting of the other patterns.

The unit cell of AgBi_4 has been reported to be either cubic (space group $Fd\bar{3}m$) or a metrically-cubic trigonal cell (space group $R\bar{3}m$).^{S4} The structure of Cu_2AgBi_6 has been reported to crystallise in a similar-sized trigonal cell with space group $R\bar{3}m$.^{S5} The structure of CuAgBi_5 has been reported to crystallise in a trigonal unit cell with space group $R\bar{3}m$ but

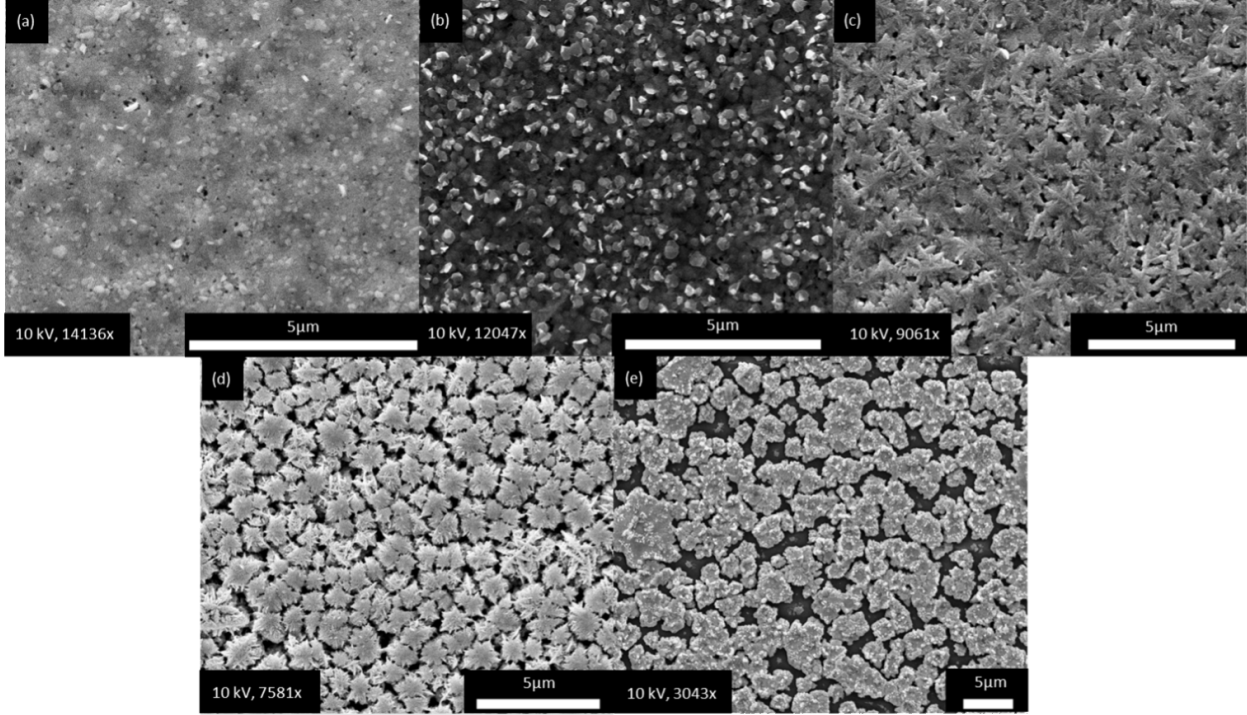


Figure S2: SEM images of $\text{Cu}_{4x}(\text{AgBi})_{1-x}\text{I}_4$ films for nominal compositions $x = 0$ (AgBiI_4), 0.09 ($\text{Cu}_{0.4}\text{AgBi}_{4.4}$), 0.2 (CuAgBiI_5), 0.33 ($\text{Cu}_2\text{AgBiI}_6$), 0.6 ($\text{Cu}_6\text{AgBiI}_{10}$) deposited on microscope slides.

with the a-lattice parameter roughly doubled compared to that of AgBiI_4 and $\text{Cu}_2\text{AgBiI}_6$.^{S6} For these reasons, in order to compare how the lattice parameters change across the series, a small trigonal unit cell with space group $R\bar{3}m$ was fitted to all the compounds apart from CuAgBiI_5 . In the graphs plotted we have halved the refined a-lattice parameter of the larger trigonal unit cell of the CuAgBiI_5 phase. Subsequently, our reported CuAgBiI_5 unit cell volume is four times smaller than as refined.

The sample corresponding to $x = 0$ (AgBiI_4) is fitted to a small trigonal cell associated with the Ag-Bi-I materials, with a small AgI impurity present.^{S4} A small trigonal cell is also fitted to the $x = 0.09$ ($\text{Cu}_{0.4}\text{AgBi}_{4.4}$) sample, along with a CuI impurity. For $x = 0.2$ (CuAgBiI_5), we fit the XRD pattern to the larger trigonal cell reported for CuAgBiI_5 ,^{S6} and a CuI impurity. Samples corresponding to $x = 0.33$ and 0.6 are fitted to a mixture of two small trigonal cells, which have been found to be $\text{Cu}_2\text{AgBiI}_6$ with a Cu_2BiI_5 impurity phase in previous reports.^{S5}

As x increases in formula $\text{Cu}_{4x}(\text{AgBi})_{1-x}\text{I}_4$, we see a monotonic decrease in the a-lattice parameter of the unit cell (see Figure S4 (a)). We also see a decrease in the c-lattice parameter for $x < 0.20$, and for $x > 0.33$, with a relatively large increase in the c-lattice parameter between $x = 0.2$ and 0.33 (Figure S4 (b)). The same trend is then also observed in the volume of the unit cell (Figure S4 (c)). We argue that this could correspond to a change in the crystal structure where the octahedral network transitions from three dimensional (3D) in CuAgBiI_5 to two dimensional (2D) in $\text{Cu}_2\text{AgBiI}_6$ following substitution of octahedral site occupancy (Ag^+ and Bi^{3+}) with tetrahedral Cu^+ .^{S6} Further, these trends also highlight the compositional change across the series, giving us confidence in attributing the measured changes in optoelectronic properties, discussed in the main text, to such compositional and structural variations. (We note that on its own, SEM-EDX would not show this as it represents the measurement of the average composition of the film, rather than of an individual phase.)

The XRD patterns of thin films deposited on glass microscope slides (deposited from the same solutions as those on quartz), were also fitted with Pawley fits (see Figure S5). We find that the phases present match those of the films deposited on the quartz substrate, and are therefore representative of the films used for optoelectronic characterisation. The films deposited on microscope slides show BiOI impurities, measured as peaks in 2θ around 9.7° , 19.2° and 39.2° , which are not seen in the films deposited on quartz and which we link to the slight iodine deficiencies measured in the compositions.

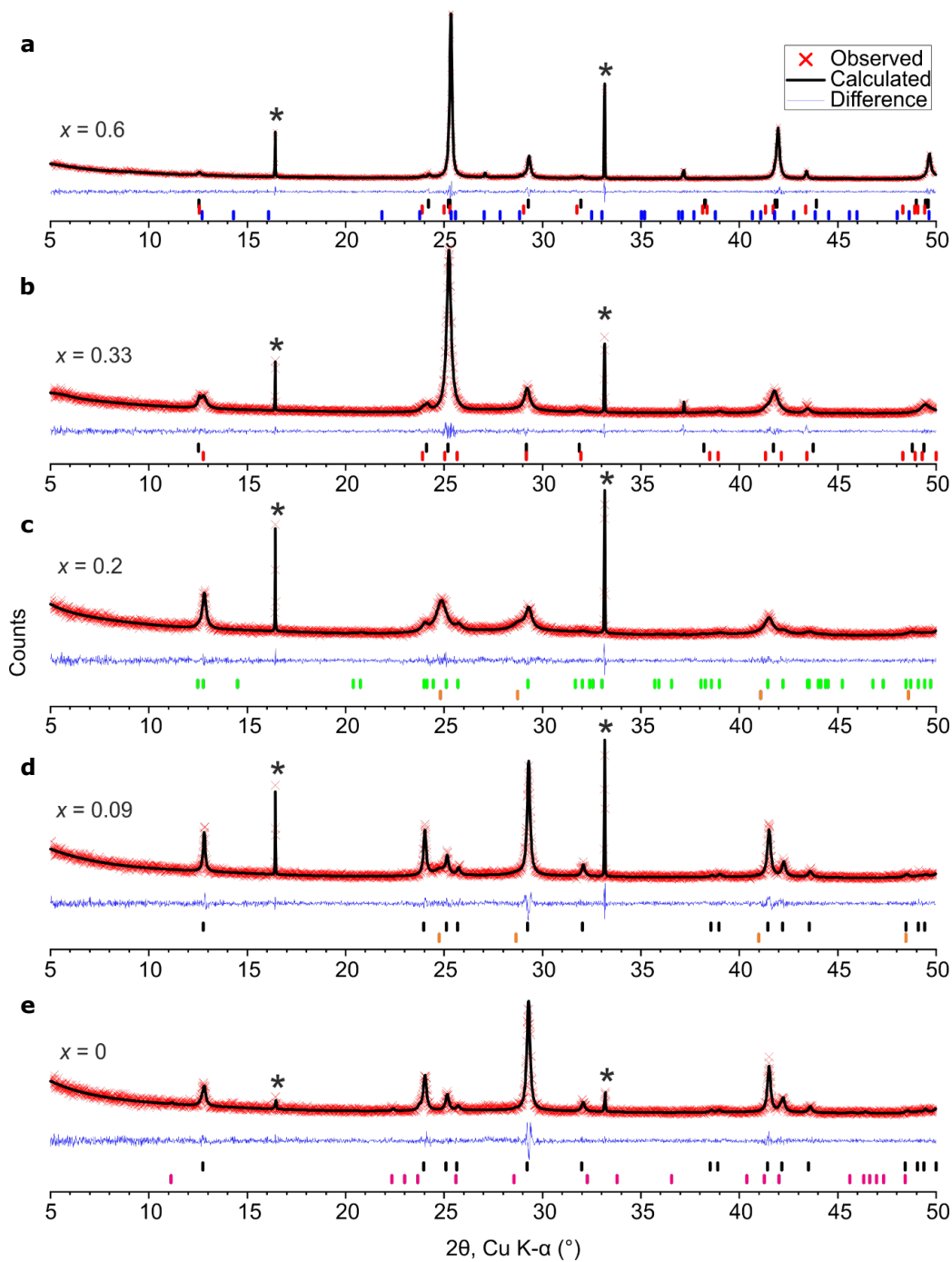


Figure S3: (a) – (e) Pawley fits to XRD patterns of $\text{Cu}_{4x}(\text{AgBi})_{1-x}\text{I}_4$ films for nominal compositions $x = 0$ (AgBiI_4), 0.09 ($\text{Cu}_{0.4}\text{AgBiI}_{4.4}$), 0.2 (CuAgBiI_5), 0.33 ($\text{Cu}_2\text{AgBiI}_6$), 0.6 ($\text{Cu}_6\text{AgBiI}_{10}$) on quartz substrates, used for optoelectronic characterisation. Black tick marks correspond to the targeted Cu-Ag-Bi-I or Ag-Bi-I phases fitted using a small trigonal cell. Tick marks of a secondary trigonal phase (most likely Cu_2BiI_5 ^{S5}), AgI, BiI_3 , and CuI are shown in red, pink, blue and orange. The tick marks associated to the large trigonal cell reported for CuAgBiI_5 are shown in green.^{S6} Asterisks mark the peaks attributed to the quartz substrates.

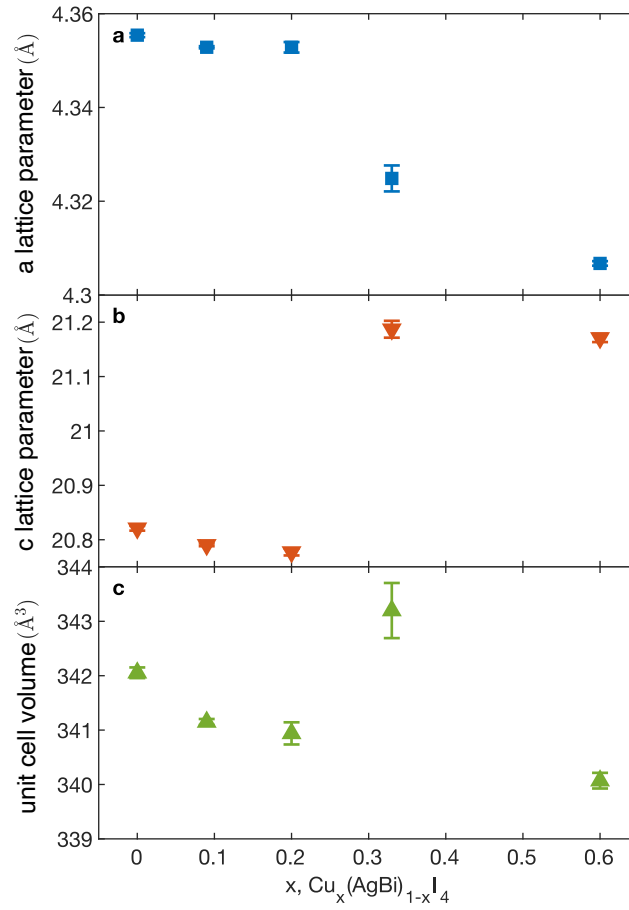


Figure S4: (a) – (c) Extracted a- and c-lattice parameters, as well as the unit cell volume, from Pawley fits to XRD patterns of $\text{Cu}_{4x}(\text{AgBi})_{1-x}\text{I}_4$ films for nominal compositions $x = 0$ (AgBiI_4), 0.09 ($\text{Cu}_{0.4}\text{AgBi}_{4.4}$), 0.2 (CuAgBiI_5), 0.33 ($\text{Cu}_2\text{AgBiI}_6$), 0.6 ($\text{Cu}_6\text{AgBiI}_{10}$). The lattice parameters were extracted from the XRD measurements taken for films on quartz substrates, as outlined above.

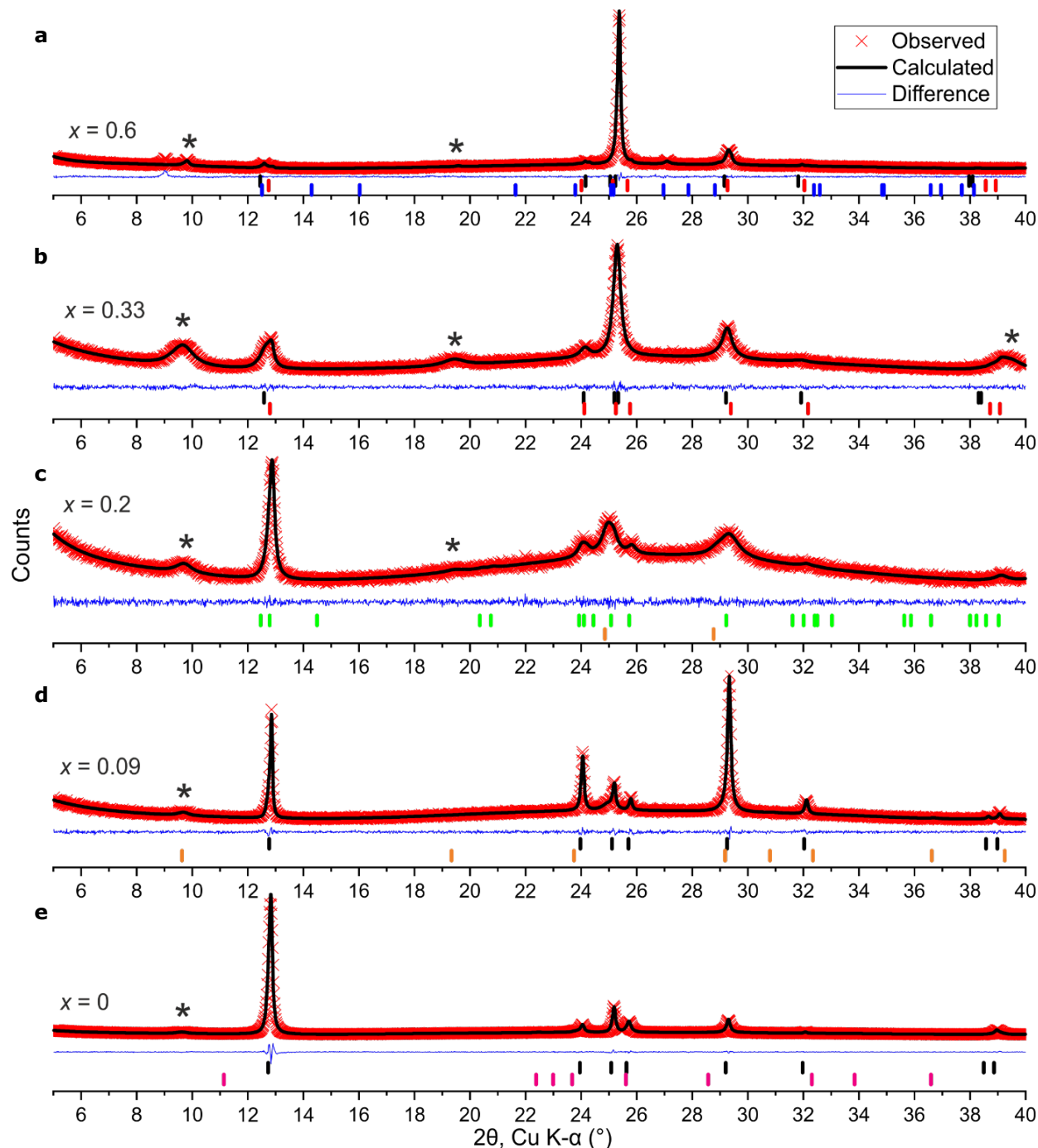


Figure S5: (a) – (e) Pawley fits to XRD patterns of $\text{Cu}_{4x}(\text{AgBi})_{1-x}\text{I}_4$ films for nominal compositions $x = 0$ (AgBiI_4), 0.09 ($\text{Cu}_{0.4}\text{AgBiI}_{4.4}$), 0.2 (CuAgBiI_5), 0.33 ($\text{Cu}_2\text{AgBiI}_6$), 0.6 ($\text{Cu}_6\text{AgBiI}_{10}$) on glass microscope slides, used for XRD and SEM measurements. Black tick marks correspond to the targeted Cu-Ag-Bi-I or Ag-Bi-I phases fitted using a small trigonal cell. Tick marks of a secondary trigonal phase (most likely Cu_2BiI_5 ^{S5}), AgI, BiI_3 , and CuI are shown in red, pink, blue and orange. The tick marks associated to the large trigonal cell reported for CuAgBiI_5 are shown in green.^{S6} The broad peaks at 9.7° , 19.2° and 39.2° , marked by asterisks, are caused by the decomposition product BiOI. There is an unidentified peak at 9° in the XRD pattern of $\text{Cu}_6\text{AgBiI}_{10}$.

4 Fitting of Optical Absorption Spectra Using Elliott's Theory

Contributions to the optical absorption of semiconductors arise from bound excitons and electron-hole continuum states. Elliott's theory can be used to describe the energy (E) dependent absorption coefficient $\alpha(E, E_G, E_B)$ arising from a semiconductor with a band gap E_G and with excitons with a binding energy E_B , and this has previously been applied to other silver-bismuth systems.^{S7} The overall absorption coefficient can thus be described as:

$$\alpha(E, E_G, E_B) = \frac{b_0}{E} \sum_{n=1}^{\infty} \frac{4\pi E_B^{3/2}}{n^3} \delta\left(E - \left[E_G - \frac{E_B}{n^2}\right]\right) + \frac{b_0}{E} \left[\frac{2\pi \sqrt{\frac{E_B}{E-E_G}}}{1 - \exp\left(-2\pi \sqrt{\frac{E_B}{E-E_G}}\right)} \right] c_0^{-1} \text{JDoS}(E) \quad (2)$$

where the joint density of states is given by $\text{JDoS}(E) = c_0 \sqrt{E - E_g}$ for $E > E_G$ and 0 otherwise, and the joint density of states constant $c_0 = \frac{1}{(2\pi)^2} \left(\frac{2\mu}{\hbar^2}\right)^{\frac{3}{2}} \times 2$, where μ is the reduced effective mass of the electron-hole system. The first term in Equation 2 contains the contribution from bound excitonic states, while the second term contains the contributions from the continuum states. Broadening caused by electron-phonon interactions, local fluctuations in the stoichiometry of the material, and energetic disorder is represented by convolution of $\alpha(E)$ with a normal distribution $\mathcal{N}(0, \Gamma^2)$ which has a mean 0 and standard deviation Γ .

The final Elliott function $f_{\text{Elliott}} = \alpha(E, E_G, E_B) * \mathcal{N}(0, \Gamma^2)$, where $*$ denotes convolution, was used to fit the optical absorption onset using a least-squares method, giving the fits shown in Figure S6 and in Main Figure 1 (b).

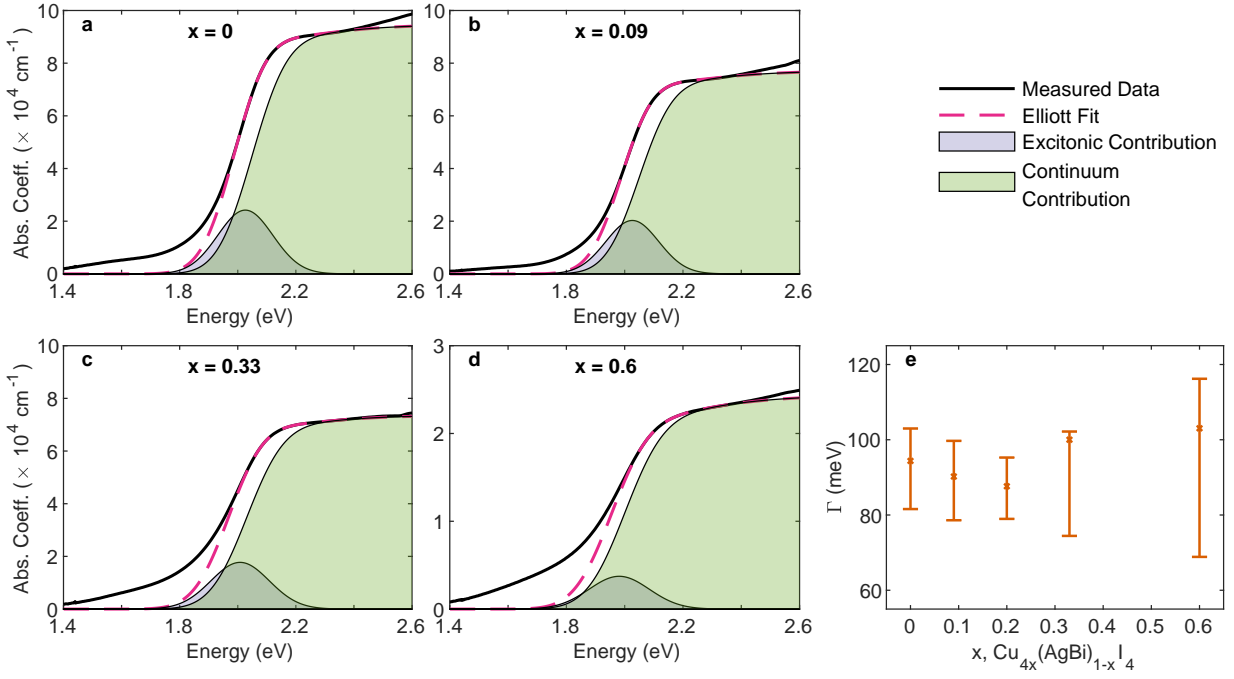


Figure S6: (a) – (d) Fits (dashed pink lines) to the steady-state optical absorption spectra (solid black lines) of $\text{Cu}_{4x}(\text{AgBi})_{1-x}\text{I}_4$ films using Elliott’s theory,^{S8} for thin films of the compositions shown in each figure. The excitonic (blue) and free-carrier contribution with Coulombic enhancement (green) are shown as the filled areas. The equivalent plot for the composition with $x = 0.2$ is shown in the main text. (e) Broadening parameter Γ obtained from the Elliott fits.

5 THz and Infra-Red Dielectric Function

Silver-bismuth-iodide lattice response is similar to that of MAPbI₃

To understand the dominant modes of the ionic lattice in these materials, terahertz absorption measurements were carried out over the range 0.5 – 2.7 THz (2.1 – 11.2 meV), from which the dielectric function ϵ can then be calculated in the THz frequency range. The real (blue) and imaginary (red) parts of ϵ are shown for the five compositions in Figure S7 (a) – (e), which show two clear phonon peaks in the imaginary part for all compositions, with fits according to a Lorentzian lineshape shown in black. (See next section below for discussion of the calculation of ϵ and of the fitting.) The outputs of the fits are the peak frequencies f_1 , f_2 peak broadenings γ_1 , γ_2 and high-frequency ($\epsilon_{\infty}^{\text{THz}}$) and static (ϵ_s^{THz}) limits of the dielectric function (relative to the THz range measured here), which are shown in Figure S7 (f) – (i) and Main Figure 1 (g).

One clear conclusion from the dielectric function fits is that any vibrational modes associated with the copper-iodide network do not feature in the THz frequency regime; the lattice response measured here must be predominantly arising from the network of silver, bismuth and iodine ions. This conclusion follows from the lack of shift in frequency of either phonon peak, which fall between 1.02 – 1.07 THz and 2.08 – 2.30 THz, including for $x = 0$, implying that the addition of copper does not alter the two phonon modes measured in this energy range.

In addition, both of the phonon modes measured here are similar to those of MAPbI₃, whose transverse optical phonon modes feature at $f_1 = 0.96$ and $f_2 = 1.96$ THz.^{S9} This observation is somewhat surprising, given the different compositions and substantially different crystal structures of the materials measured here (edge-sharing, partially layered octahedra of the materials measured here vs. corner-sharing, fully connected octahedra in MAPbI₃). If we consider the simplified example of a diatomic chain, two factors determine the phonon mode frequency: the ‘spring constant’, i.e. the strength of the ionic bonds in the lattice; and

the reduced mass of the ions in the chain. On its own, the slightly higher mass of bismuth, relative to lead, would imply a red-shifted frequency. However, the difference in electronegativity between iodine (2.66) and bismuth (2.02) is larger than that between iodine and lead (2.33):^{S10} given that the strength of an ionic bond depends on the *difference* between the electronegativities of the two ions, a Bi-I bond will be more ionic than a Pb-I bond, leading to a higher phonon frequency. We measure phonon frequencies here that are slightly above those measured for MAPbI₃, implying that the change in electronegativity dominates the change in mass, leading to the small blue-shift in f_1 and f_2 . (We also note that silver-iodine modes should be found at higher frequencies, outside of the range measured here, given the combination of a much lower ionic mass for Ag⁺ as well as an even lower electronegativity (1.93^{S10}) than bismuth, both of which would blue-shift the frequency substantially.)

Finally, lattice modes influence the polarisation of the ionic lattice, which in turn influences how photoexcited charges are screened in a semiconductor. The blue shift in phonon modes, relative to MAPbI₃, brings their energy closer to E_B , and thus should lead to increased screening of the Coulombic attraction between electrons and holes, reducing E_B .^{S11,S12} However, the binding energy also depends generally on the electron-hole reduced mass M and dielectric screening as $E_B \propto \frac{M}{\epsilon}$. As discussed in the main text, we find the values of the high-frequency ($\epsilon_\infty^{\text{THz}}$) limit of the dielectric function (relative to the THz range) to all be similar to, or slightly above, the value for MAPbI₃ ($\epsilon_\infty^{\text{THz}} \sim 5.4$ ^{S12}) at its exciton binding energy. Given that the exciton binding energies measured here are all at least 50% higher than that determined for MAPbI₃, we think this is likely caused by a larger reduced mass, rather than any reduction in dielectric screening in the silver-bismuth materials studied here. Further, the correlation of lowered exciton binding energies and increased charge-carrier mobilities with rising x also indicates this to be the dominant trend (rather than the lack of correlation of E_B with values of ϵ across the compositional series).

On the whole, the combination of similar phonon modes and values of the dielectric function show that the underlying ionic lattice in the silver-bismuth materials investigated here

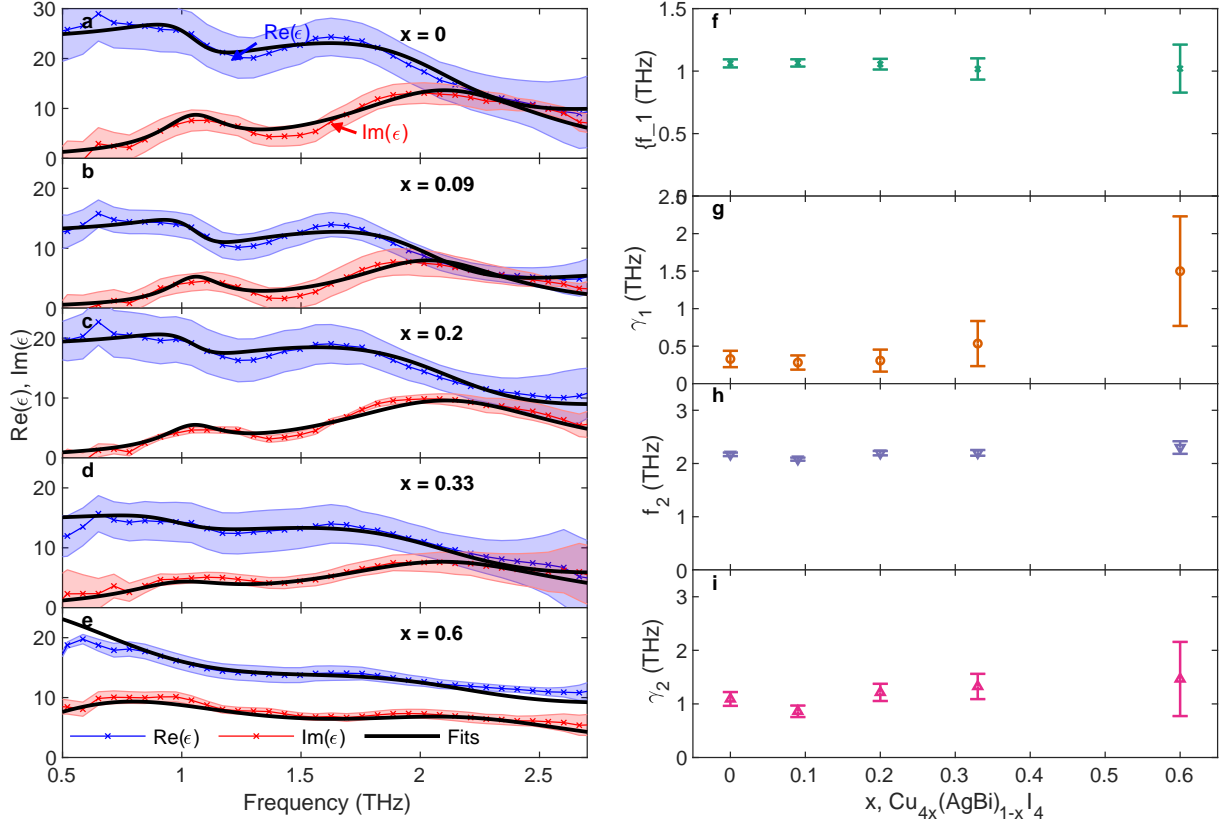


Figure S7: (a) – (e) Measured real (blue) and imaginary (red) parts of the dielectric function in the THz frequency range for thin films of the five compositions measured. Every composition shows two clear phonon peaks in the imaginary part, at approximately 1.1 and 2.2 THz. The black lines are fits to the dielectric function using a two-peak Lorentzian line shape. (See main text of the SI for a detailed discussion of the fitting and outputs.) (f) Fitted frequency f_1 of the lower-energy phonon peak. (g) Fitted broadening parameter γ_1 of the lower-energy phonon peak. (h) Fitted frequency f_2 of the higher-energy phonon peak. (i) Fitted broadening parameter γ_2 of the higher-energy phonon peak. (j) Values of the high-frequency (red) and static (cream) dielectric constants for each composition.

is comparable to that of conventional metal-halide perovskites such as MAPbI₃, notwithstanding the variations in crystal structure and composition.

5.1 Calculation and modelling of dielectric function in the THz frequency range

THz transmission measurements were carried out for each Cu_{4x}(AgBi)_{1-x}I₄ film, as well as for a blank 2 mm-thick z-cut quartz substrate, used as a reference. This approach allows for

the calculation of $T(\omega) = E_{\text{sam}}(\omega)/E_{\text{ref}}(\omega)$. Further, in order to account for variations in the thickness of the z-cut quartz substrates, a phase factor was included, giving the following final expression for $T(\omega)$:

$$T(\omega) = \frac{E_{\text{sam}}(\omega)}{E_{\text{ref}}(\omega)} e^{\frac{-i\Delta d(n_s-1)\omega}{c}}, \quad (3)$$

where $\Delta d = d_{\text{sam}} - d_{\text{ref}}$, $n_s = 2.13$ is the refractive index of quartz in the THz frequency regime,^{S1} and c is the speed of light.

In this case where the thin-film of $\text{Cu}_{4x}(\text{AgBi})_{1-x}\text{I}_4$ has a thickness much less than the wavelength in the THz range (i.e. $d_{\text{sam}} \ll \lambda_{\text{THz}}$) and the underlying substrate is thicker than the wavelength in the THz range (i.e. $d_{\text{ref}} > \lambda_{\text{THz}}$), the dielectric function in vacuum can then be calculated as:^{S13}

$$\epsilon(\omega) = \frac{ic(1+n_s)}{\omega d_{\text{sam}}} \left(\frac{1}{T(\omega)} - 1 \right) + 1. \quad (4)$$

The dielectric response of a material can be modelled through Lorentzian fitting of the spectra as the sum of contributions from n phonon modes that are present in the measured spectral range, and the high-frequency response ϵ_∞ :

$$\epsilon(\omega) = \sum_{i=1}^n \epsilon_{\text{ph}}^{(i)}(\omega) + \epsilon_\infty. \quad (5)$$

Here the contribution from each phonon mode can be modelled as a Lorentzian oscillator, which results in the following expression for the Drude-Lorentz dielectric response:^{S14}

$$\epsilon_{\text{ph}}(\omega) = -\Delta\epsilon_s \frac{\omega_0^2}{\omega^2 - \omega_0^2 + i\gamma\omega}, \quad (6)$$

where $\Delta\epsilon_s$ is the contribution of the phonon mode to the static (zero-frequency) value of the dielectric function, ω_0 is its (angular) resonance frequency, and γ is its broadening parameter (half line width).

The overall static value of the dielectric function, in our case with two phonon modes present, can thus be calculated as:

$$\epsilon_s = \epsilon_\infty + \Delta\epsilon_s^1 + \Delta\epsilon_s^2. \quad (7)$$

The fitted values of f_1 , γ_1 , f_2 , γ_2 , ϵ_∞ and ϵ_s are shown in Figure S7 and Main Figure 1 (g). Fits were carried out between 0.5 – 2.7 THz.

We note that the correction to account for Δd leads to variations in the final shape of the real and imaginary parts of the dielectric function, and thus to the values obtained from the fits. As has been shown elsewhere,^{S15} variations in the value of Δd lead to very minor changes in the imaginary part of the dielectric function (and thus in the values of f_1 , γ_1 , f_2 , γ_2), but influence the real part of the dielectric function more substantially (and thus the values of ϵ_∞ and ϵ_s).

To properly account for this uncertainty, we cross-verified our results in two ways in order to ensure physical consistency. First, we measured the thickness of the quartz substrates used for each sample, and for the reference measurements, using a micrometer. This gave an average thickness of $d = 2.0210 \pm 0.0005$ mm. Given that the measured error is equal to $0.5 \mu\text{m}$, we thus calculated and fitted the dielectric function for each sample with three values of $\Delta d = -0.5, 0, +0.5 \mu\text{m}$.

Second, we used the values of the dielectric constant in the infra-red, ϵ^{IR} , as a lower bound for the value of $\epsilon_\infty^{\text{THz}}$ (see below for calculation), as any dielectric function responses between ~ 1300 nm (0.95 eV) and 2.5 THz (120 μm or 0.01 eV), for example owing to phonon resonances, would increase the value of the real part of the dielectric function and thus increase both $\epsilon_\infty^{\text{THz}}$ and ϵ_s^{THz} .^{S12}

Figure S8 shows an example plot of the real and imaginary parts of the THz dielectric function for AgBiI_4 ($x = 0$) for the three values of Δd , with the corresponding fits (including a lower limit for the value of $\epsilon_\infty^{\text{THz}} = \epsilon^{\text{IR}}$ from the UV-visible transmission measurements). The variations in Δd lead to substantial variations in $\epsilon_\infty^{\text{THz}}$ and ϵ_s^{THz} (apparent in the real

part of the dielectric function), whereas the peak positions and broadenings vary little (as shown in the imaginary part of the dielectric function).

The spectra shown in Figure S7 are all calculated for $\Delta d = 0 \mu\text{m}$. Then, for the THz dielectric values shown in Main Figure 1 (g), we use the values obtained from the fits with $\Delta d = -0.5, +0.5 \mu\text{m}$ as the upper and lower error bounds for the values of $\epsilon_{\infty}^{\text{THz}}$ and ϵ_s^{THz} . Instead, for the phonon peak frequencies and broadenings shown in Figure S7, we show the errors obtained from the fitting procedure with $\Delta d = 0 \mu\text{m}$, as these are larger.

5.2 Calculation of the dielectric function in the infra-red

In order to calculate the values of the dielectric function in the infra-red region, ϵ^{IR} , we fitted the measured values of R, T between 1200 – 1300 nm from the UV-Visible absorption measurements with values of R and T calculated from Fresnel coefficients, accounting for Fabry-Perot interference inside the thin film sample,^{S11} of the stack of layers vacuum-sample-quartz-vacuum. This approach allows for the extraction of the values of the refractive index and dielectric function in the infra-red frequency range.

In general, the Fresnel reflection and transmission coefficients $r_{i,j}$ and $t_{i,j}$ of the electric field, for normal incidence going from layer i to layer j , are given by:^{S11}

$$r_{i,j} = \frac{n_i - n_j}{n_i + n_j} \quad (8)$$

and

$$t_{i,j} = \frac{2n_i}{n_i + n_j}. \quad (9)$$

Then, we define the Fabry-Perot interference term inside the sample as:

$$F = \frac{1}{1 - r_{\text{sam,vac}} r_{\text{sam,sub}} \exp\left(\frac{2i\omega d_{\text{sam}} n_{\text{sam}}}{c}\right)}. \quad (10)$$

For the total reflection from the stack, we thus obtain:

$$r_{\text{Tot}} = r_{\text{vac,sam}} + t_{\text{vac,sam}} \exp\left(\frac{2i\omega d_{\text{sam}} n_{\text{sam}}}{c}\right) F r_{\text{sam,sub}} t_{\text{sam,vac}}. \quad (11)$$

Here $d_{\text{sam}}, n_{\text{sam}}$ are the thickness and refractive index of the sample, and we use values of 1 and 1.54 for the refractive indices of vacuum and z-cut quartz. We then calculate the total reflected intensity as $R = |r|^2$, where we have assumed that the silver mirror reference used for reflection is 100% reflective in the 1200 – 1300 nm range, as was the case for the UV-visible absorption measurements carried out.

Instead, for the transmission through the stack the relevant expression is:

$$t_{\text{Tot}} = t_{\text{vac,sam}} \exp\left(\frac{i\omega d_{\text{sam}} n_{\text{sam}}}{c}\right) F t_{\text{sam,sub}} \exp\left(\frac{i\omega d_{\text{sub}} n_{\text{sub}}}{c}\right) t_{\text{sub,vac}}. \quad (12)$$

Here $d_{\text{sub}} = 2$ mm and $n_{\text{sub}} = 1.54$ are the thickness and refractive index of the z-cut quartz substrate. We also calculate the transmission through a vacuum-quartz-vacuum stack:

$$t_{\text{Ref}} = t_{\text{vac,sub}} \exp\left(\frac{i\omega d_{\text{sub}} n_{\text{sub}}}{c}\right) t_{\text{sub,vac}}. \quad (13)$$

The total transmitted intensity is then calculated as $T = |t_{\text{Tot}}/t_{\text{Ref}}|^2$, which accounts for the reference measurement through a blank quartz substrate, as outlined above.

The Fresnel coefficients depend on the refractive index n of the sample, which in turn depends on ϵ as:

$$n = \sqrt{\epsilon} + i\kappa, \quad (14)$$

where κ is the absorption coefficient (fixed to be the measured value for each sample).

We thus fit the measured values of R, T in the 1200 – 1300 nm range with values calculated as above, allowing the value of ϵIR to vary, whilst fixing all other relevant parameters. This fitting routine yield the values of ϵIR found in Main Figure 1 (g), which represents values of the dielectric function in the IR, sub-bandgap part of the spectrum. We note that this

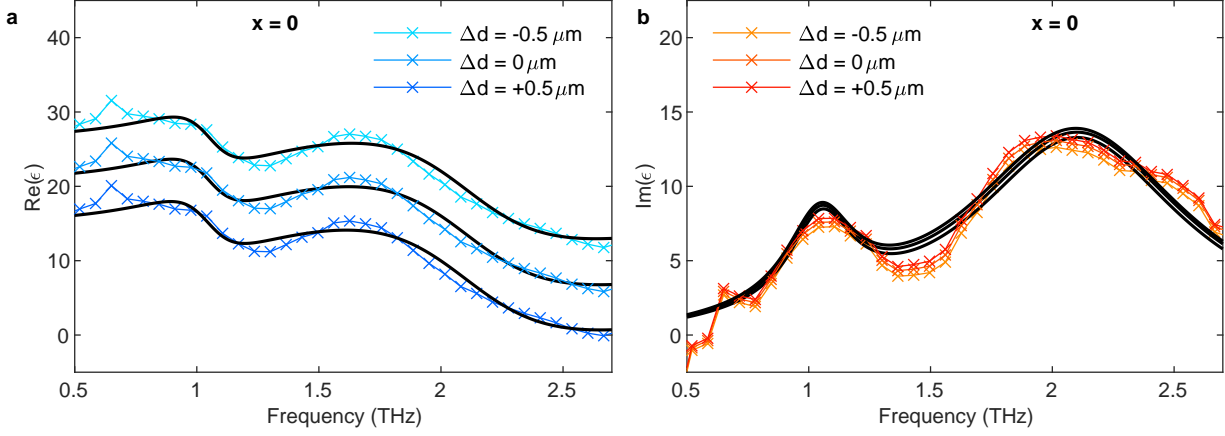


Figure S8: (a) Real part of the dielectric function in the THz frequency range for a thin film of AgBiI_4 , calculated using values of $\Delta d = -0.5, 0, +0.5 \mu\text{m}$ for the variations in substrate thickness (lighter to darker shades of blue, fits in black). Changing the value of Δd leads to substantial vertical offsets in the real part of the dielectric function, influencing the values of $\epsilon_{\infty}^{\text{THz}}$ and ϵ_s^{THz} . (b) Imaginary part of the dielectric function in the THz frequency range, calculated using values of $\Delta d = -0.5, 0, +0.5 \mu\text{m}$ (lighter to darker shades of red, fits in black). Variations in Δd do not lead to substantial variations in phonon peak frequencies or broadenings.

approximation does not account for internal reflections in the quartz, as these would add high-frequency oscillations that are not resolved by the instrument used for the measurements.

6 PL Stability Under Continuous Illumination

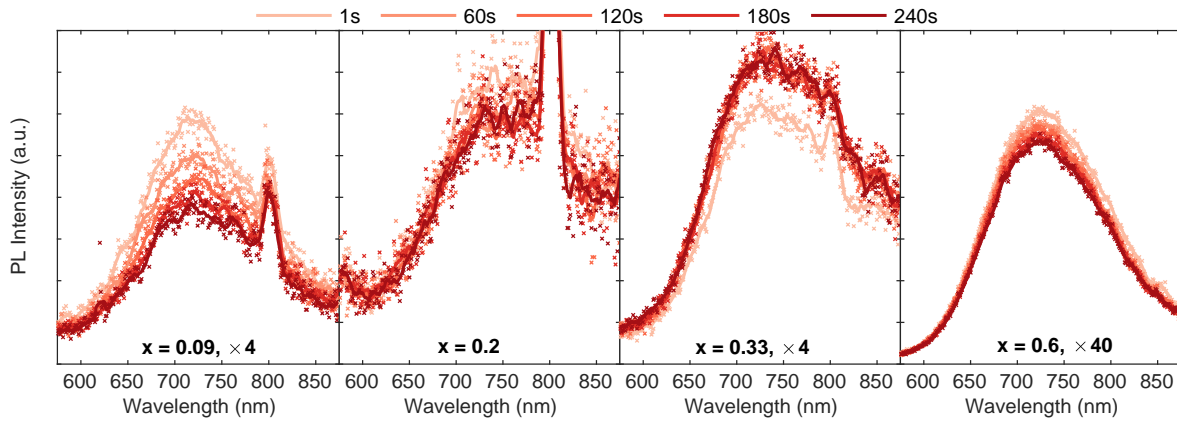


Figure S9: (a) – (d) Measured PL spectra under continuous illumination over 240s at 41 Wcm^{-2} for four thin films of $\text{Cu}_{4x}(\text{AgBi})_{1-x}\text{I}_4$ with the x values shown. The spectra measured after 1, 60, 120, 180, 240s are shown as crosses, and the solid lines are a ten-point moving average. The spectra show small changes in intensity, but no change in spectra shape, over the 240s for all compositions.

7 Photoluminescence and Time-Correlated Single-Photon Counting

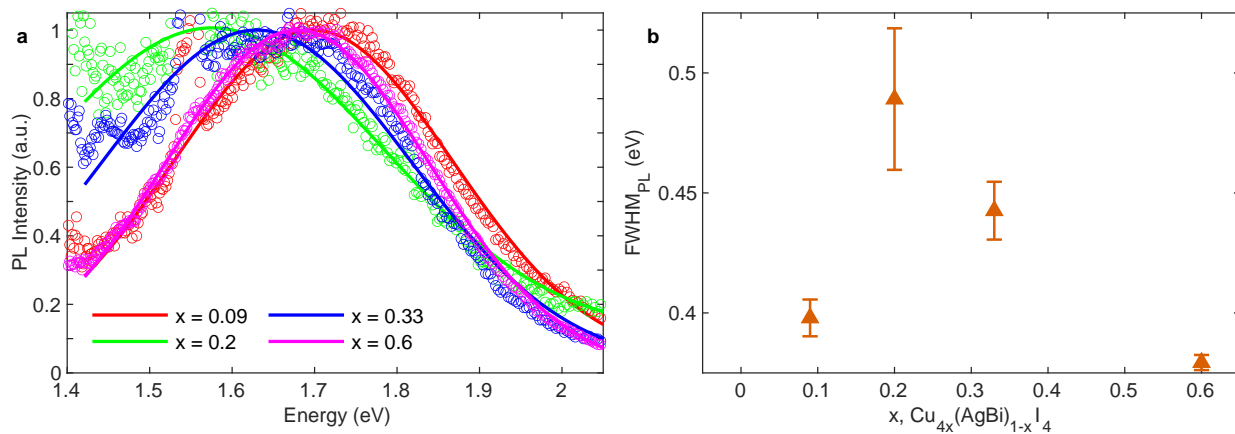


Figure S10: (a) Normalised photoluminescence spectra of $\text{Cu}_{4x}(\text{AgBi})_{1-x}\text{I}_4$ films, measured following excitation at 398nm with a continuous-wave intensity of 265 Wcm^{-2} . Measured spectra are shown as open circles, Gaussian fits as solid lines. (b) Full-width half-maxima extracted from the Gaussian fits to the photoluminescence spectra.

Steady-state photoluminescence (PL) spectra were fitted with a Gaussian lineshape with the form:

$$\text{PL} = A \exp\left(-\left(\frac{E - E_0}{\sigma}\right)^2\right) + B. \quad (15)$$

Here A is the PL amplitude, E_0 is the PL peak energy, σ is the width of the Gaussian and B is an offset along the y-axis. The value of the full-width at half maximum was then calculated as $\text{FWHM} = \sigma 2\sqrt{2 \log 2}$. The normalised fits and resulting FWHM values are shown in Figure S10.

In order to understand whether the dynamics of the PL emission are influenced by composition, we carried out further time-resolved PL measurements of the emission bands between 1.58 – 1.70 eV. Such measurements were carried out on $\text{Cu}_{4x}(\text{AgBi})_{1-x}\text{I}_4$ thin films following photoexcitation at 398 nm at fluences of 440 and 1580 nJcm^{-2} using time-correlated single-photon counting, the results of which are shown in Figure S10 (a) – (e). (Because of this technique’s greater sensitivity than the iCCD used for the steady-state measurements, we were able to record PL transient decays for AgBiI_4 .) The lower-fluence decays were then fitted with a stretched exponential of the form $I = I_0 e^{-(\frac{t}{\tau_{\text{char}}})^\beta}$, and an average lifetime was calculated as $\tau_{\text{av}} = \frac{\tau_{\text{char}}}{\beta} \Gamma(\frac{1}{\beta})$, where Γ is the gamma function.^{S16} From the average lifetime, we then calculate a monomolecular (trap-mediated) recombination rate $k_1 = 1/(2\tau_{\text{av}})$, following the convention of Richter et al,^{S17} the values of which are plotted in Figure S10 (f).

The recombination rates are all between $0.27 - 1.46 \times 10^9 \text{ s}^{-1}$, somewhat higher than those found in conventional lead-halide perovskites,^{S18} but comparable to defect-heavy tin-based perovskites,^{S19,S20} which together with values of β that are well below 1 (i.e. substantial heterogeneity in the decays, see Figure S10 (g)), is indicative of a large trap density and substantial energetic disorder present in these materials. The lack of clear trend in the defect-mediated, nanosecond charge-carrier recombination rate k_1 with composition again demonstrates that the ultrafast charge-carrier localisation taking place in these silver-bismuth materials, which exhibits clear trends across the series, has an intrinsic nature.

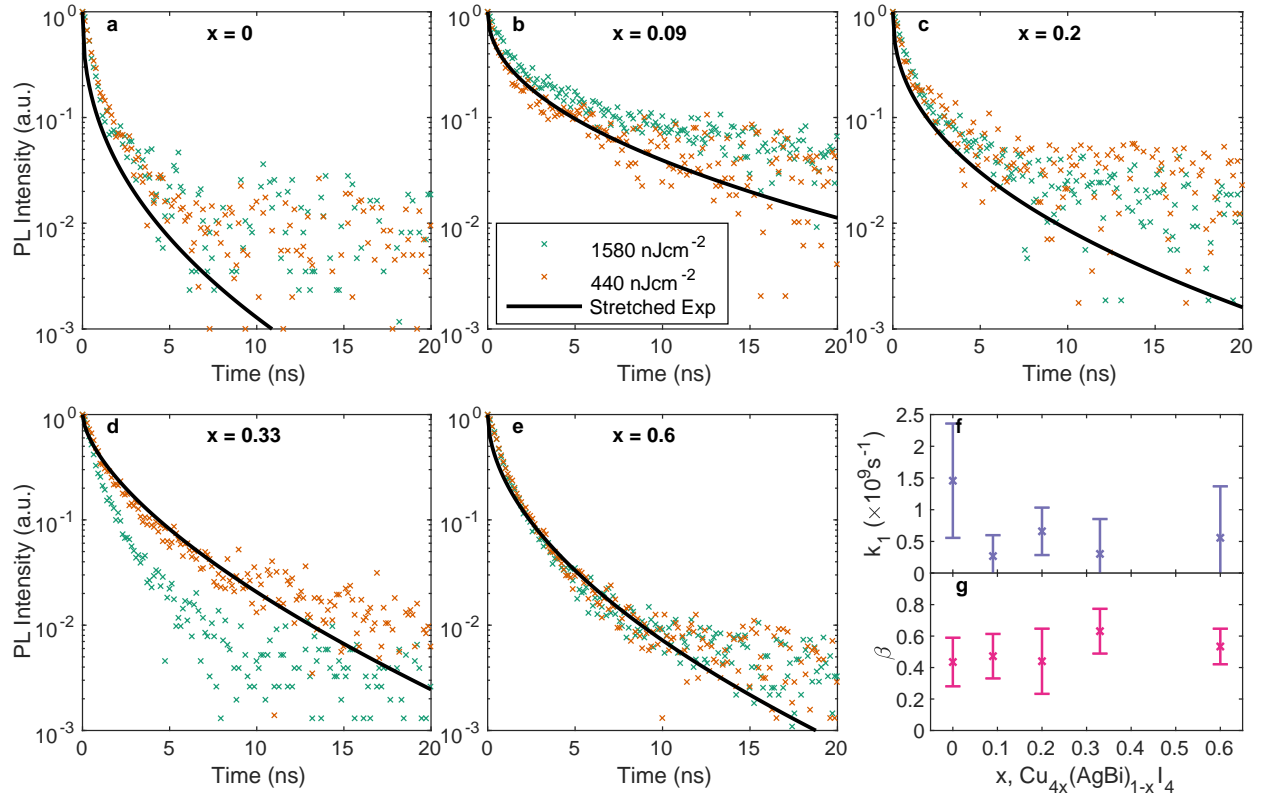


Figure S11: (a) – (e) Time-resolved PL transients measured using TCSPC at fluences of 1580 and 440 nJcm^{-2} , for $\text{Cu}_{4x}(\text{AgBi})_{1-x}\text{I}_4$ thin films of the compositions shown. The solid black lines are fits using a stretched exponential. (f) Monomolecular recombination rate k_1 extracted from the fits, and also plotted as solid blue squares in Main Figure 5 (a). (g) Homogeneity parameter β extracted from the fits.

8 THz Photoconductivity

Drude Factor Calculation

To investigate the nature of the photoinduced charge carriers we measured photoconductivity spectra across the range of 0.25 – 2.5 THz following photoexcitation at 3.1 eV at a fluence of $49 \mu\text{Jcm}^{-2}$ across several time delays (see Figure S12 (a) – (e)). The photoconductivity spectra exhibit reasonably flat real parts, indicative of Drude-like conductivity, typical of free charge carriers.^{S13,S21} The lack of resonance peaks is indicative of a lack of optically allowed transitions in the energy range 1 – 10 meV (0.25 – 2.5 THz), in good agreement with the exciton binding energies measured here (the first excitonic transition would be expected at an energy of $\frac{3}{4}E_B \geq 16 \text{ meV}$). In order to quantify deviations from Drude-like conductivity, we calculate a ‘Drude Factor’ (see below), as done previously for other metal-halide semiconductors,^{S22,S23} for each composition at several time delays (see Figure S12 (a) – (e)). These values show no trend over time for all compositions, although the time-averaged values are somewhat below 1, falling in the range 0.67 – 0.69, indicating some degree of deviation from the idealised charge-carrier transport of free electrons. Further, the time-averaged Drude Factor increases slightly with x (Figure S12 (f)), which could be correlated with the improved charge-carrier mobilities that we discuss below.

The Drude model for the photoconductivity of a electrons in a solid yields a flat, zero-valued imaginary part of the photoconductivity in the THz regime.^{S13,S14,S21} In order to quantify deviations from this model, a ‘Drude Factor’ can be calculated as:^{S22}

$$f_{\text{Drude}} = \frac{1}{x} \sum_1^x \frac{\sqrt{\text{Re}(\Delta T/T)^2}}{\sqrt{\text{Re}(\Delta T/T)^2 + \text{Im}(\Delta T/T)^2}}. \quad (16)$$

Here $\Delta T/T = \frac{T_{\text{On}} - T_{\text{Off}}}{T_{\text{Off}}}$ is the change in THz transmission at each frequency point, and x is the total number of points (in this case, we calculated f_{Drude} between 0.4 – 2.5 THz). In the case of ideal Drude-like conductivity, $f_{\text{Drude}} = 1$, and deviations indicate other contributions

e.g. from localized charge-carrier states.^{S21}

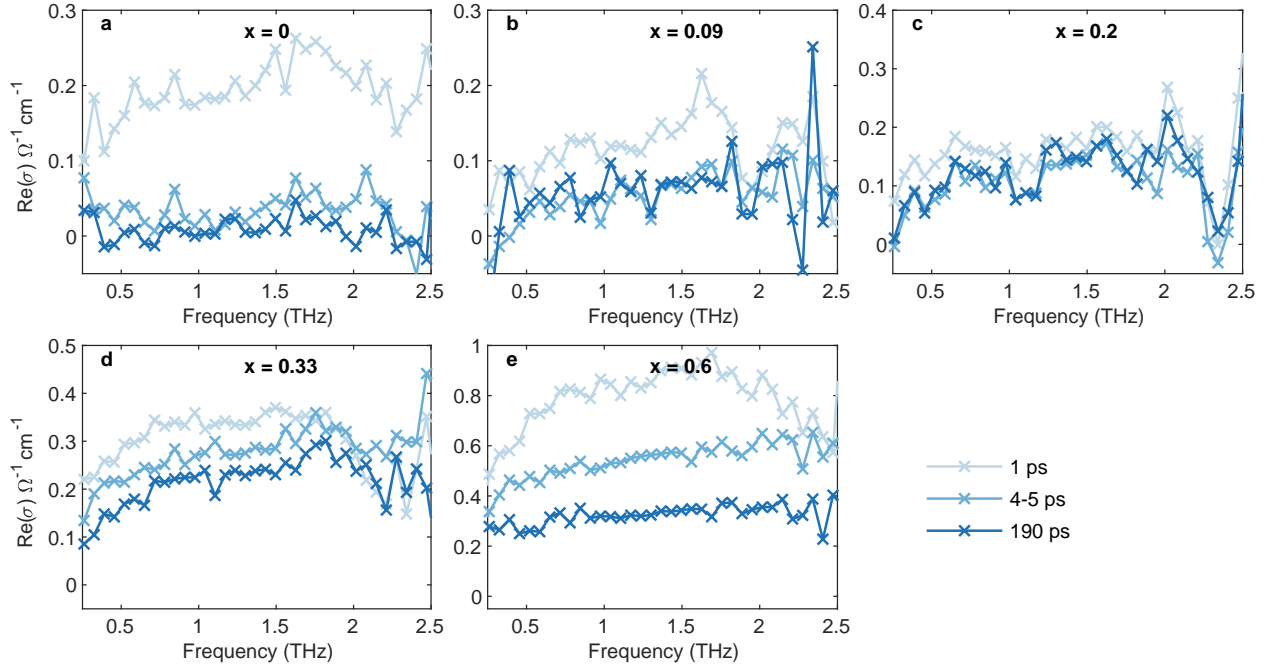


Figure S12: (a) – (e) Real part of the photoconductivity measured for $\text{Cu}_{4x}(\text{AgBi})_{1-x}\text{I}_4$ thin films of copper content x as shown, at time delays of 1, 4-5 and 190 ps. The spectra were measured following photoexcitation with a pump wavelength of 400 nm at a fluence of $49 \mu\text{Jcm}^{-2}$ (incident photon fluxes of $N_A = 9.9 \times 10^{13} \text{cm}^{-2}$, as calculated below).

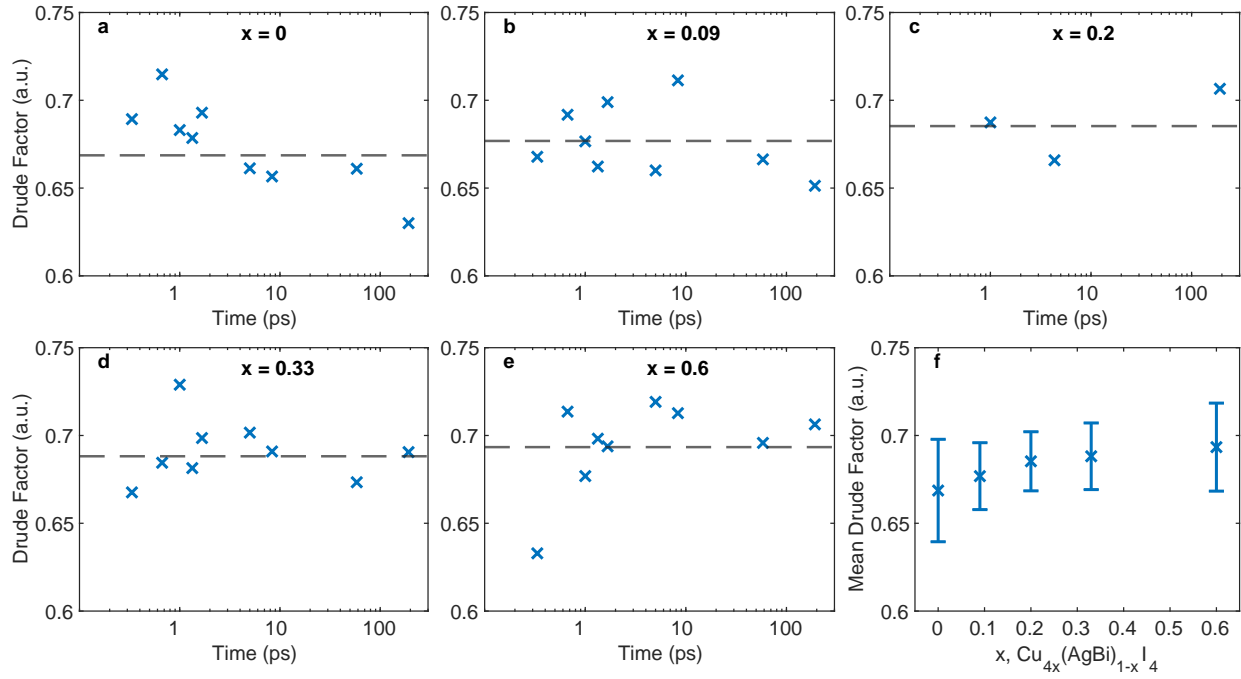


Figure S13: (a) – (e) Calculated ‘Drude Factor’ for thin films with the compositions shown, at a variety of time delays following photoexcitation at 400 nm at a fluence of $49 \mu\text{Jcm}^{-2}$ (incident photon fluxes of $N_A = 9.9 \times 10^{13} \text{ cm}^{-2}$, as calculated below). None of the compositions show any clear trend over time, although the average values calculated over all times (f) show a slight increase in value with increasing x .

9 Fitting of OPTP Decays

This section discusses the ordinary differential equation (ODE)-based models used to fit the OPTP transients, over long and early times. This model is shown schematically in Main Figure 3 (e).

Early-time OPTP fitting

In order to fit the early-time OPTP transients, we follow the same approach used in previous studies.^{S7,S23}

We assume that all photoexcited carriers begin in the free state, such that $n_{\text{deloc}}(t = 0) = n_0$ and $n_{\text{loc}}(t = 0) = 0$. For each pump wavelength, the initial charge-carrier density was calculated as:

$$N = \frac{E\lambda}{hc} (1 - R_{\text{pump}}(\lambda) - T_{\text{pump}}(\lambda)), \quad (17)$$

where E is the energy contained in an optical excitation pulse of wavelength λ , and R_{pump} and T_{pump} are the sample reflectivity and transmittance at the pump wavelength λ . In order to convert this into a charge-carrier density per unit volume, we accounted for the effective overlap area of the optical pump and THz probe beams and the thickness of the sample, such that:

$$n_0 = \frac{N}{d_{\text{film}} A_{\text{Eff}}}. \quad (18)$$

The recombination rate from the localised state to the ground state, k_1^* , is fixed using the values of k_1 and k_2 obtained from the long-time fits (see below). We note that, as discussed in the main text, we do not identify the precise nature of the localized or self-trapped state (e.g. a self-trapped hole or exciton, or a small polaron), and so the schematic is simply representative of the states and the parameters associated with them, and should not be

interpreted as a band structure or energy-level diagram.

The simplified model outlined can thus be solved using a set of coupled rate equations:

$$\frac{\partial n_{\text{deloc}}}{\partial t} = -k_{\text{loc}} n_{\text{deloc}} \quad (19)$$

$$\frac{\partial n_{\text{loc}}}{\partial t} = -k_1^* n_{\text{loc}} + k_{\text{loc}} n_{\text{deloc}}. \quad (20)$$

As outlined previously,^{S7} $\Delta T/T$ can be related to the photoinduced change in the conductivity, and the overall measured signal can then be described using the following analytical form:

$$\frac{\Delta T}{T} = \frac{-n_0 e d}{\epsilon_0 c (n_A + n_B)} \left(\left(\mu_{\text{deloc}} - \frac{\mu_{\text{loc}} k_{\text{loc}}}{k_{\text{loc}} - k_1^*} \right) e^{-k_{\text{loc}} t} + \frac{\mu_{\text{loc}} k_{\text{loc}}}{k_{\text{loc}} - k_1^*} e^{-k_1^* t} \right). \quad (21)$$

In order to account for the Instrument Response Function of the OPTP system used here (see below), the expression in Equation 21 was convolved with a normalised Gaussian pulse with $\sigma_{\text{IRF}} = 0.32$ ps. Accounting for an offset in time t_0 , the overall expression used to fit the temperature-dependent OPTP data was thus:

$$\frac{\Delta T}{T}(t-t_0) = \frac{-en_0 d_{\text{film}}}{2\epsilon_0 c(n_A + n_B)} \left\{ \left(\mu_{\text{deloc}} - \frac{\mu_{\text{loc}} k_{\text{loc}}}{k_{\text{loc}} - k_1^*} \right) e^{-k_{\text{loc}}(t-t_0) + \frac{k_{\text{loc}}^2 \sigma_{\text{IRF}}^2}{2}} \text{Erfc} \left(\frac{k_{\text{loc}} \sigma_{\text{IRF}}^2 - (t-t_0)}{\sqrt{2} \sigma_{\text{IRF}}} \right) + \frac{\mu_{\text{loc}} k_{\text{loc}}}{k_{\text{loc}} - k_1^*} e^{-k_1^*(t-t_0) + \frac{k_1^{*2} \sigma^2}{2}} \text{Erfc} \left(\frac{k_1^* \sigma_{\text{IRF}}^2 - (t-t_0)}{\sqrt{2} \sigma_{\text{IRF}}} \right) \right\}. \quad (22)$$

Here $\text{Erfc}(x)$ is the complementary error function, defined as:

$$\text{Erfc}(x) = \frac{2}{\sqrt{\pi}} \int_x^\infty e^{-t^2} dt \quad (23)$$

The fits were carried out for each pump wavelength, globally across all fluences at that wavelength, yielding values of μ_{deloc} , μ_{loc} and k_{loc} at the three wavelengths, for each sample.

These fit outputs are shown in Main Figures 3 and 4.

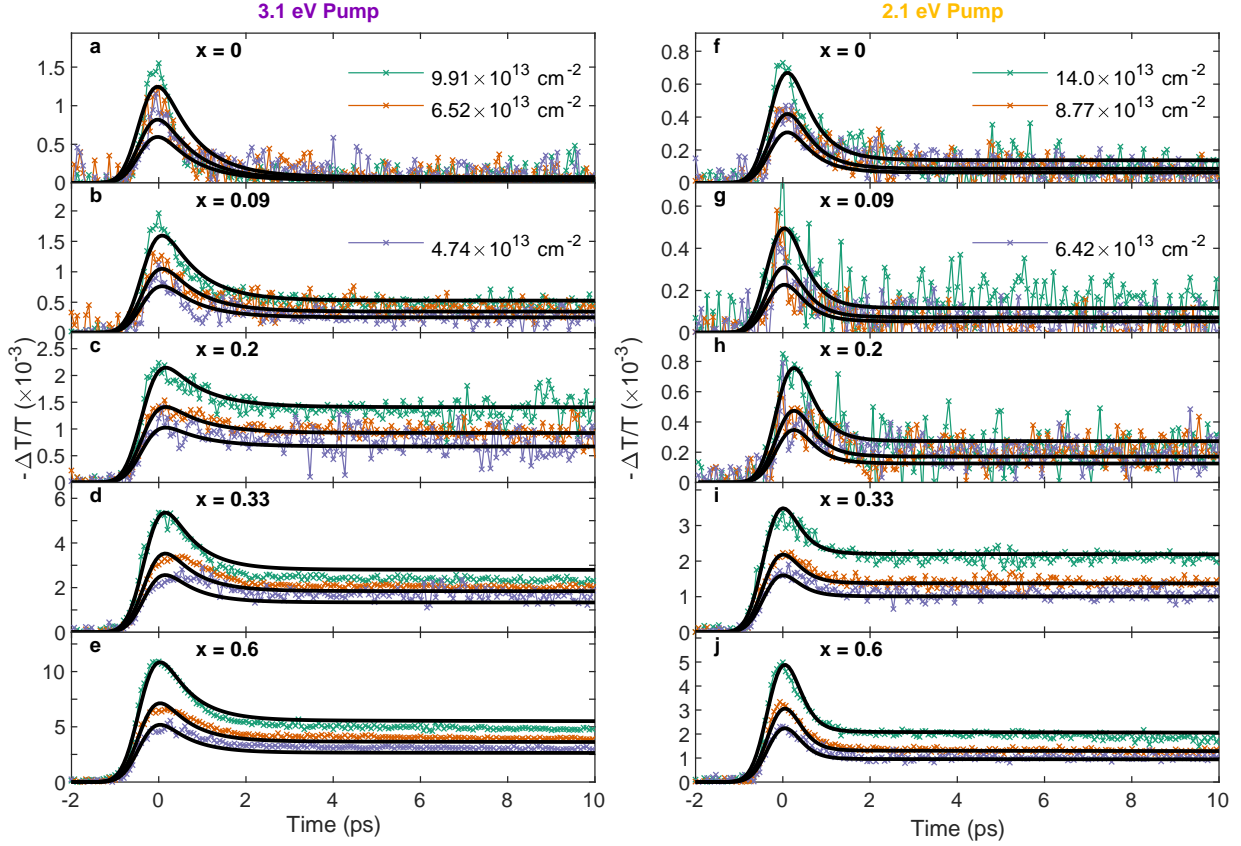


Figure S14: (a) – (e) OPTP photoconductivity transients between -2 – 10 ps for thin films with the five $\text{Cu}_{4x}(\text{AgBi})_{1-x}\text{I}_4$ compositions shown, using photoexcitation at 3.1 eV with incident photon fluxes of $N_A = 9.91, 6.52, 4.74 \times 10^{13} \text{ cm}^{-2}$. The solid black lines are fits to the decays as outlined above. (f) – (j) OPTP transient decays between -2 – 10 ps for thin films with the five compositions shown, using photoexcitation at 585 nm with incident photon fluxes of $N_A = 14.0, 8.77, 6.42 \times 10^{13} \text{ cm}^{-2}$. The solid black lines are fits to the decays as outlined above.

Long-time (nanosecond) OPTP fitting

The long-time fits over approximately the first nanosecond follow the same approach we have outlined previously.^{S24} We assume that recombination dynamics of the charge carriers from the localised state can be described by a combination of monomolecular (trap-mediated) and bimolecular (radiative) recombination, giving the following rate equation:

$$\frac{\partial n}{\partial t} = -k_1 n - k_2 n^2. \quad (24)$$

This solution to this equation is given by:

$$n(t) = \frac{k_1 \alpha}{e^{k_1 t} - k_2 \alpha} \quad (25)$$

where α is related the initial charge-carrier density n_0 via:

$$\frac{1}{\alpha} = \frac{k_1}{n_0} + k_2. \quad (26)$$

The change in transmitted THz radiation, $\frac{\Delta T}{T}(t) \equiv x(t)$ is proportional to the free charge-carrier density in the thin film:

$$n(t) = \phi C x(t) \quad (27)$$

Here ϕ is the number of free charge-carriers per photon, and $C = \tilde{n}_0/x(0)$ is the proportionality factor between the initial THz response $x(0)$ and the absorbed photon density n_0 .

Substituting for C then gives us:

$$\frac{\partial x}{\partial t} = -C\phi k_2 x^2 - k_1 x \quad (28)$$

$$= -A_2 x^2 - A_1 x \quad (29)$$

Analytical solutions to this ODE are fitted globally to the decays across all fluences in order to extract the rate constants A_i . Given the influence of the photon-to-free-charge conversion ratio ϕ we can only determine apparent bimolecular recombination rates ϕk_2 . Just as for the charge-carrier mobilities shown above, given that $0 \leq \phi \leq 1$ the values presented for k_2 in the main text are underestimates of the true intrinsic values.

Finally, in order to account for an initial spatially varying charge-carrier density (due to absorption following the Beer-Lambert law), the fitting algorithm takes into account an

exponentially decaying charge-carrier density. This is done by dividing the sample into 30 equally thick slices and computing the decay function for each of these individually.

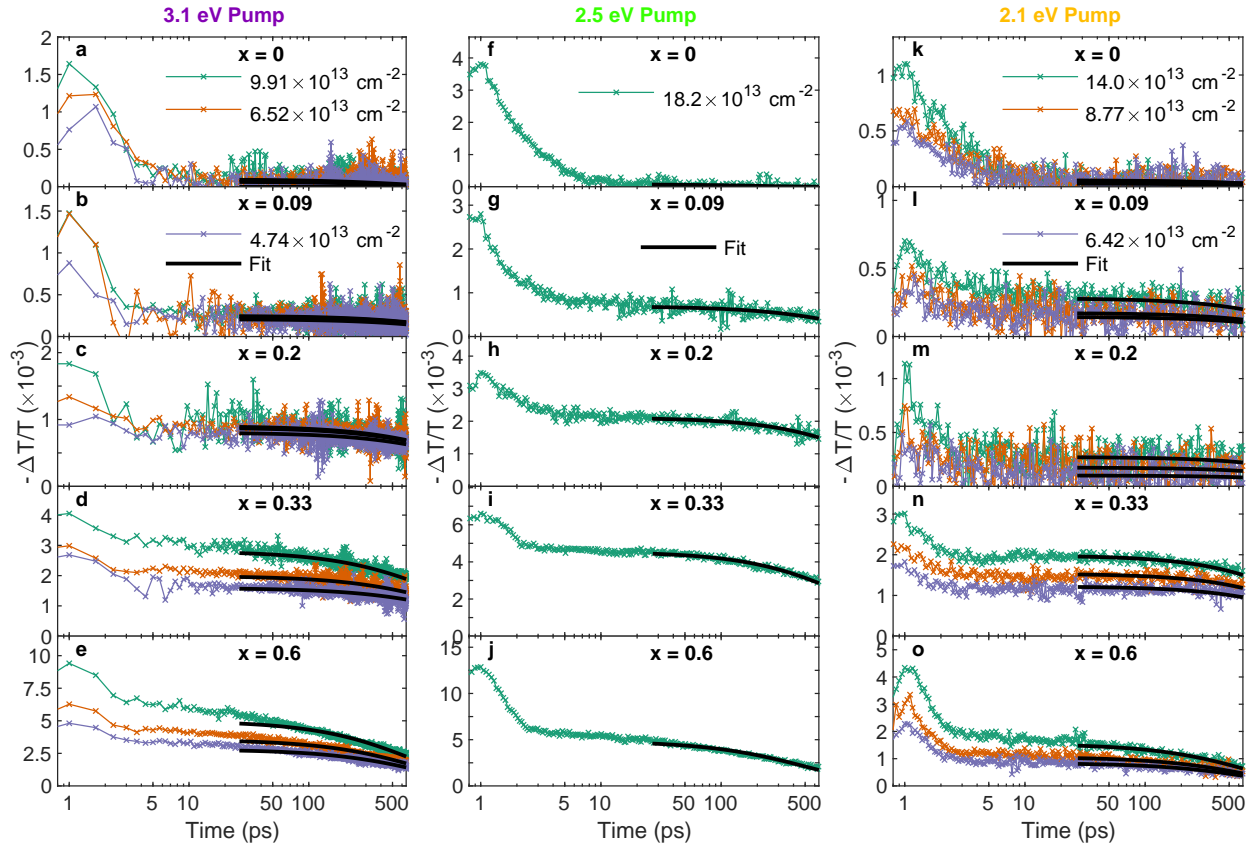


Figure S15: (a) – (e) OPTP transients covering the first 600 ps, for thin films with the five $\text{Cu}_{4x}(\text{AgBi})_{1-x}\text{I}_4$ compositions shown, following photoexcitation at 3.1 eV with incident photon fluxes of $N_A = 9.91, 6.52, 4.74 \times 10^{13} \text{ cm}^{-2}$. The solid black lines are fits to the decays as outlined above. (f) – (j) OPTP transient decays out to 600 ps for thin films with the five compositions shown, using photoexcitation at 2.5 eV with incident photon flux of $N_A = 18.2 \times 10^{13} \text{ cm}^{-2}$. The solid black lines are fits to the decays as outlined above. (k) – (o) OPTP transients out to 600 ps for thin films with the five compositions shown, using photoexcitation at 2.1 eV with incident photon fluxes of $N_A = 14.0, 8.77, 6.42 \times 10^{13} \text{ cm}^{-2}$. The solid black lines are fits to the decays as outlined above. For ease of comparison, all decays have been shifted along the time axis such that their peak values are at $t = 1$ ps.

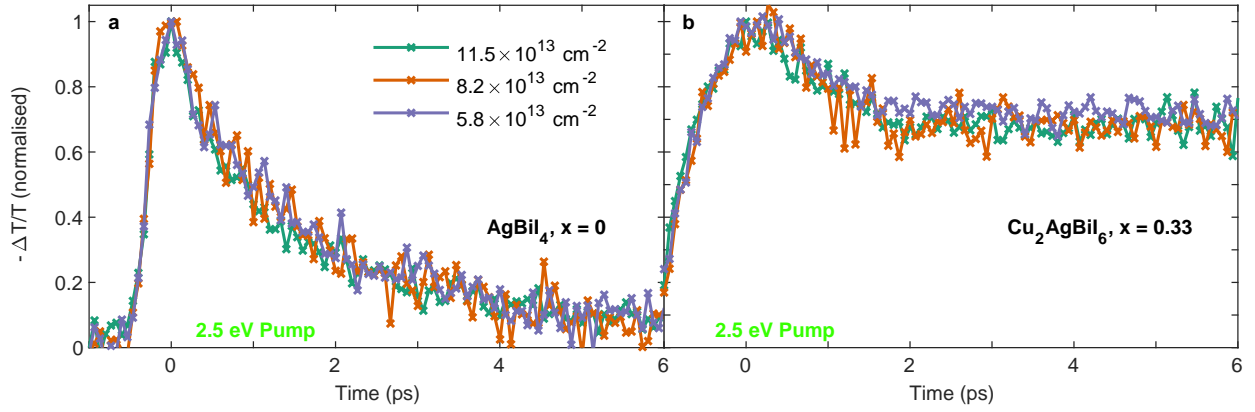


Figure S16: Normalised OPTP transient decays between $-1 - 6$ ps for thin films of AgBiI_4 (a) and $\text{Cu}_2\text{AgBiI}_6$ (b), following photoexcitation at 2.5 eV with incident photon fluxes of $N_A = 11.5, 8.2, 5.8 \times 10^{13} \text{ cm}^{-2}$. The transients show very little difference, implying a lack of fluence dependence to the dynamics at early times. For clarity, the decays have all been shifted along the x-axis such that the peak is at time $t = 0$ ps.

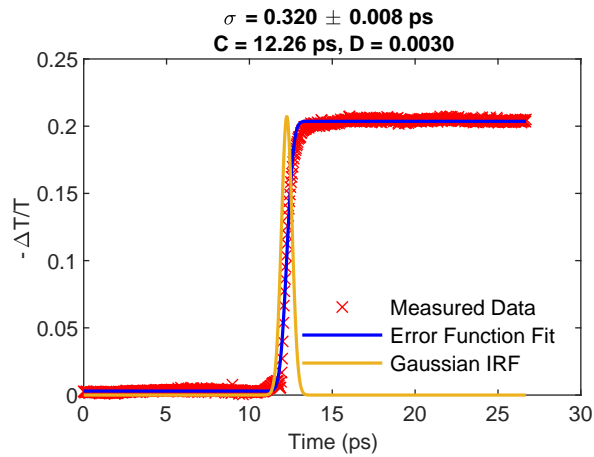


Figure S17: Early-time OPTP onset for a 2 mm-thick wafer of high-resistivity silicon, pumped at 800 nm at a fluence of $17.7 \mu\text{Jcm}^{-2}$. The data are fitted with an error function in order to extract an estimate of the instrument response function of our OPTP system. The resulting Gaussian IRF has a spread of 320 fs, much shorter than the dynamics observed in the thin films measured here.

10 Instrument Response of OPTP Spectroscopy

As a measure of the Instrument Response Function (IRF) of our THz OPTP spectroscopy systems, high-resolution measurements of the photoconductivity onset in silicon were carried out. These data are then fitted with an error function, via an equation of the form:

$$F(x) = A(1 - \text{Erf}(B(x - C))) + D \quad (30)$$

where A , B , C and D are fitting constants and the error function is defined as:

$$\text{Erf}(x) = \frac{2}{\sqrt{\pi}} \int_0^x e^{-t^2} dt. \quad (31)$$

This timing is then converted into a Gaussian temporal broadening to simulate the IRF of our experimental system:

$$G(x) = \alpha e^{-\left(\frac{x-\beta}{\sqrt{2}\sigma_{\text{IRF}}}\right)^2} \quad (32)$$

where the constant σ_{IRF} is related to the fitted value B by $\sigma_{\text{IRF}} = 1/(\sqrt{2}B)$, α is the amplitude and β is the offset in time (equivalent to C).

This approach yields the IRF shown in SI Figure S17, with $\sigma_{\text{IRF}} = 320$ fs, much faster than the timescales for the ultrafast localisation k_{loc} that are shown in Main Figure 3 (c).

11 Fluences, Photon Fluxes and Photoexcited Charge-Carrier Densities for OPTP Measurements

We report below in Table S2 the fluence (energy per unit area) and photon flux for each set of OPTP measurements reported here, as well as the corresponding photo-excited charge-carrier density used for each $\text{Cu}_{4x}(\text{AgBi})_{1-x}\text{I}_4$ composition.

The photoexcitation fluence is calculated as:

$$F = \frac{P}{f A_{\text{eff}}}, \quad (33)$$

where P is the power of the photoexcitation pump beam, f is the repetition rate of the pump beam (5 kHz, as reported above) and A_{eff} is the effective overlap area between the optical pump and THz probe beams.

The incident photon flux can then be calculated as:

$$N_{\text{A}} = \frac{F\lambda}{hc} \quad (34)$$

where λ is the photoexcitation wavelength, h is Planck's constant and c is the speed of light.

Finally, for a given thin film and incident photon flux, the photoexcited charge-carrier density can be calculated as:

$$n_0 = \frac{N_{\text{A}}(1 - R_{\text{pump}}(\lambda) - T_{\text{pump}}(\lambda))}{d_{\text{film}}} \quad (35)$$

where $R_{\text{pump}}(\lambda)$, $T_{\text{pump}}(\lambda)$ are the reflectance and transmittance at the photoexcitation wavelength λ , and d_{film} is the thickness of the thin film.

Nominal x and $\text{Cu}_{4x}(\text{AgBi})_{1-x}\text{I}_4$ Composition	Pump Energy (eV)	Pump Fluence (μJcm^{-2})	Incident Photon Flux ($\times 10^{13} \text{ cm}^{-2}$)	Photoexcited Charge- Carrier Density ($\times 10^{18} \text{ cm}^{-3}$)
0, AgBiI_4	3.1	49.2	9.91	2.54
		32.4	6.52	1.67
		23.5	4.74	1.21
	2.5	72.44*	18.2*	4.68*
		45.8	11.5	2.96
		32.6	8.21	2.11
		21.8	5.81	1.49
	2.1	47.5	14.0	3.50
		29.8	8.77	2.20
		21.8	6.42	1.61
0.09, $\text{Cu}_{0.4}\text{AgBiI}_{4.4}$	3.1	49.2	9.91	2.07
		32.4	6.52	1.36
		23.5	4.74	0.99
	2.5	72.44*	18.2*	3.76*
		45.8	11.5	2.37
		32.6	8.21	1.69
		21.8	5.81	1.20
	2.1	47.5	14.0	2.78
		29.8	8.77	1.74
		21.8	6.42	1.28
0.2, CuAgBiI_5	3.1	49.2	9.91	2.19
		32.4	6.52	1.44
		23.5	4.74	1.05
	2.5	72.44*	18.2*	3.90*
		45.8	11.5	2.46
		32.6	8.21	1.75
		21.8	5.81	1.24

Nominal x and $\text{Cu}_{4x}(\text{AgBi})_{1-x}\text{I}_4$ Composition	Pump Energy (eV)	Pump Fluence (μJcm^{-2})	Incident Photon Flux ($\times 10^{13} \text{ cm}^{-2}$)	Photoexcited Charge- Carrier Density ($\times 10^{18} \text{ cm}^{-3}$)	
0.33, $\text{Cu}_2\text{AgBiI}_6$	2.1	47.5	14.0	2.86	
		29.8	8.77	1.79	
		21.8	6.42	1.31	
	0.6, $\text{Cu}_6\text{AgBiI}_{10}$	3.1	49.2	9.91	2.28
			32.4	6.52	1.50
			23.5	4.74	1.09
		2.5	72.44*	18.2*	4.16*
			45.8	11.5	2.63
			32.6	8.21	1.87
2.1		47.5	14.0	3.13	
		29.8	8.77	1.96	
		21.8	6.42	1.44	
0.6, $\text{Cu}_6\text{AgBiI}_{10}$	3.1	49.2	9.91	1.15	
		32.4	6.52	0.75	
		23.5	4.74	0.55	
	2.5	72.44*	18.2*	1.99*	
		45.8	11.5	1.26	
		32.6	8.21	0.90	
	2.1	47.5	14.0	1.46	
		29.8	8.77	0.91	
		21.8	6.42	0.67	

Table S2: Photoexcitation fluences, incident photon fluxes and photoexcited charge-carrier densities for each $\text{Cu}_{4x}(\text{AgBi})_{1-x}\text{I}_4$ composition for the early- and long-time OOTP measurements. For photoexcitation at 3.1 and 2.1 eV, the same three fluences were used for both early- and long-time decay measurements. For photoexcitation at 2.5 eV, only one fluence (marked with an asterisk *) was used for the long-time decay measurements, whilst the three lower fluences were used for the early-time decay measurements.

References

- (S1) Davies, C. L.; Patel, J. B.; Xia, C. Q.; Herz, L. M.; Johnston, M. B. Temperature-Dependent Refractive Index of Quartz at Terahertz Frequencies. *Journal of Infrared, Millimeter, and Terahertz Waves* **2018**, *39*, 1236–1248.
- (S2) Seifert, T.; Jaiswal, S.; Martens, U.; Hannegan, J.; Braun, L.; Maldonado, P.; Freimuth, F.; Kronenberg, A.; Henrizi, J.; Radu, I.; Beaurepaire, E.; Mokrousov, Y.; Oppeneer, P. M.; Jourdan, M.; Jakob, G.; Turchinovich, D.; Hayden, L. M.; Wolf, M.; Münzenberg, M.; Kläui, M.; Kampfrath, T. Efficient metallic spintronic emitters of ultrabroadband terahertz radiation. *Nature Photonics* **2016**, *10*, 483–488.
- (S3) d’Amour, H.; Denner, W.; Schulz, H. Structure determination of α -quartz up to 68×10^8 Pa. *Acta Crystallographica Section B Structural Crystallography and Crystal Chemistry* **1979**, *35*, 550–555.
- (S4) Sansom, H. C.; Whitehead, G. F.; Dyer, M. S.; Zanella, M.; Manning, T. D.; Pitcher, M. J.; Whittles, T. J.; Dhanak, V. R.; Alaria, J.; Claridge, J. B.; Rosseinsky, M. J. AgBiI₄ as a Lead-Free Solar Absorber with Potential Application in Photovoltaics. *Chemistry of Materials* **2017**, *29*, 1538–1549.
- (S5) Sansom, H. C.; Longo, G.; Wright, A. D.; Buizza, L. R. V.; Zanella, M.; Gibbon, J. T.; Abda-Jalebi, M.; Pitcher, M. J.; Dyer, M. S.; Manning, T. D.; Dhanak, V. R.; Friend, R. H.; Herz, L. M.; Snaith, H. J.; Claridge, J. B.; Rosseinsky, M. J. Highly Absorbing Lead-Free Semiconductor Cu₂AgBiI₆ for Photovoltaic Applications from the Quaternary CuI–AgI–BiI₃ Phase Space. *Journal of the American Chemical Society* **2021**, *143*, 3983–3992.
- (S6) Sansom, H. C.; Buizza, L. R. V.; Zanella, M.; Gibbon, J. T.; Pitcher, M. J.; Dyer, M. S.; Manning, T. D.; Dhanak, V. R.; Herz, L. M.; Snaith, H. J.; Claridge, J. B.; Rosseinsky, M. J. Chemical Control of the Dimensionality of the Octahedral Network

- of Solar Absorbers from the CuI-AgI-BiI₃ Phase Space by Synthesis of 3D CuAgBiI₅. *ACS Inorganic Chemistry* **2021**, *Accepted for Publication*.
- (S7) Wright, A. D.; Buizza, L. R. V.; Savill, K. J.; Longo, G.; Snaith, H. J.; Johnston, M. B.; Herz, L. M. Ultrafast Excited-State Localization in Cs₂AgBiBr₆ Double Perovskite. *Journal of Physical Chemistry Letters* **2021**, *12*, 3352.
- (S8) Elliott, R. J. Intensity of optical absorption by excitons. *Physical Review* **1957**, *108*.
- (S9) Wehrenfennig, C.; Liu, M.; Snaith, H. J.; Johnston, M. B.; Herz, L. M. Charge-carrier dynamics in vapour-deposited films of the organolead halide perovskite CH₃NH₃PbI_{3-x}Cl_x. *Energy Environ. Sci.* **2014**, *7*, 2269–2275.
- (S10) Allred, A. L. Electronegativity values from thermochemical data. *Journal of Inorganic and Nuclear Chemistry* **1961**, *17*, 215–221.
- (S11) Fox, M. *Optical Properties of Solids*, 2nd ed.; Oxford University Press, 2010.
- (S12) Herz, L. M. How lattice dynamics moderate the electronic properties of metal-halide perovskites. *Journal of Physical Chemistry Letters* **2018**, *9*, 6853–6863.
- (S13) Ulatowski, A. M.; Herz, L. M.; Johnston, M. B. Terahertz Conductivity Analysis for Highly Doped Thin-Film Semiconductors. *Journal of Infrared, Millimeter, and Terahertz Waves* **2020**, *41*, 1431–1449.
- (S14) Yu, P. Y.; Cardona, M. *Fundamentals of semiconductors : physics and materials properties*, 4th ed.; Springer: Heidelberg Dordrecht London New York, 2010.
- (S15) La-O-Vorakiat, C.; Cheng, L.; Salim, T.; Marcus, R. A.; Michel-Beyerle, M. E.; Lam, Y. M.; Chia, E. E. Phonon features in terahertz photoconductivity spectra due to data analysis artifact: A case study on organometallic halide perovskites. *Applied Physics Letters* **2017**, *110*, 123901.

- (S16) Johnston, D. C. Stretched exponential relaxation arising from a continuous sum of exponential decays. *Physical Review B* **2006**, *74*, 184430.
- (S17) Richter, J. M.; Abdi-Jalebi, M.; Sadhanala, A.; Tabachnyk, M.; Rivett, J. P.; Pazos-Outón, L. M.; Gödel, K. C.; Price, M.; Deschler, F.; Friend, R. H. Enhancing photoluminescence yields in lead halide perovskites by photon recycling and light out-coupling. *Nature Communications* **2016**, *7*, 13941.
- (S18) Johnston, M. B.; Herz, L. M. Hybrid perovskites for photovoltaics: charge-carrier recombination, diffusion, and radiative efficiencies. *Accounts of Chemical Research* **2016**, *49*, 146–154.
- (S19) Klug, M. T.; Milot, R. L.; Patel, J.; Green, T.; Sansom, H. C.; Farrar, M.; Ramadan, A. J.; Martani, S.; Wang, Z.; Wenger, B.; Ball, J. M.; Langshaw, L.; Petrozza, A.; Johnston, M. B.; Herz, L. M.; Snaith, H. Metal composition influences optoelectronic quality in mixed-metal lead-tin triiodide perovskite solar absorbers. *Energy & Environmental Science* **2020**, *13*, 1776–1787.
- (S20) Savill, K. J.; Ulatowski, A. M.; Farrar, M. D.; Johnston, M. B.; Snaith, H. J.; Herz, L. M. Impact of Tin Fluoride Additive on the Properties of Mixed Tin-Lead Iodide Perovskite Semiconductors. *Advanced Functional Materials* **2020**, 2005594.
- (S21) Joyce, H. J.; Baig, S. A.; Parkinson, P. A review of the electrical properties of semiconductor nanowires: insights gained from terahertz conductivity spectroscopy The influence of surfaces on the transient terahertz conductivity and electron mobility of GaAs nanowires. *Semicond. Sci. Technol* **2016**, *31*, 103003.
- (S22) Milot, R. L.; Eperon, G. E.; Snaith, H. J.; Johnston, M. B.; Herz, L. M. Temperature-dependent charge-carrier dynamics in $\text{CH}_3\text{NH}_3\text{PbI}_3$ perovskite thin films. *Advanced Functional Materials* **2015**, *25*, 6218–6227.

- (S23) Buizza, L. R. V.; Wright, A. D.; Longo, G.; Sansom, H. C.; Xia, C. Q.; Rosseinsky, M. J.; Johnston, M. B.; Snaith, H. J.; Herz, L. M. Charge-Carrier Mobility and Localization in Semiconducting $\text{Cu}_2\text{AgBiI}_6$ for Photovoltaic Applications. *ACS Energy Lett.* **2021**, *6*, 1729–1739.
- (S24) Buizza, L.; Crothers, T.; Wang, Z.; Patel, J.; Milot, R.; Snaith, H.; Johnston, M.; Herz, L. Charge-Carrier Dynamics, Mobilities, and Diffusion Lengths of 2D–3D Hybrid Butylammonium–Cesium–Formamidinium Lead Halide Perovskites. *Advanced Functional Materials* **2019**, *29*.